FACHHOCHSCHULE GIESSEN FRIEDBERG
UNIVERSITY OF APPLIED SCIENCES

Fraunhofer USA Center for Laser Technology

FUNDAMENTAL STUDY IN MICROJOINING OF FUSED SILICA UTILIZING LASER RADIATION

PECULIARITIES AND POSSIBLE PROBLEMS EXEMPLIFIED AT THE PROCESS OF MANUFACTURING A FIBER CONNECTOR

A thesis submitted for the degree of Diplom-Ingenieur (FH)

Fachhochschule Giessen – Friedberg
University of Applied Sciences
Fachbereich MND
Studiengang Physikalische Technik

Examiner: Prof.Dr.rer.nat. Klaus Behler
Second examiner: Dr.-Ing. Stephan Heinemann

May 18, 2005
Marburg, Germany

Abstract

A laser micro joining process for the radial geometry of a fused silica fiber connector is developed. The special characteristics of fused silica are described and their importance for the process is evaluated. The heat flow in the glass is simulated mathematically and the results of welding experiments are discussed. The peculiarities of the radial geometry of the joint enforces a process, using the fiber as filler material to fill a gap in the seam.

Ein Lasermikroschweißprozess für die radiale Geometrie eines Quarzglas Fasersteckers wird entwickelt. Die speziellen Charakteristika von Quarzglas werden beschrieben und ihre Wichtigkeit für den Prozess bewertet. Der Wärmefluss im Glas wird mathematisch simuliert und Ergebnisse der Schweißexperimente diskutiert. Die Besonderheiten der radialen Geometrie der Verbindung erzwingen einen Prozess, bei dem die Faser als Füllstoff für einen Spalt in der Naht verwendet wird.

Acknowledgements

Working at the Fraunhofer Center for Laser Technology in Plymouth has been a remarkable experience.

I would like to thank Fraunhofer USA and in particular Dr.-Ing. Stefan Heinemann for giving me the opportunity to write my diploma thesis here and providing me with everything I needed for my work.

Thanks to Professor Dr. Klaus Behler for establishing contact to Fraunhofer USA, supervising my diploma thesis and supporting my work.

A special note of appreciation goes to Dipl.-Ing. Reiner Witte, with whom I worked closely and who supported me in every way during my work. It was his and Dipl.-Ing Hans Herfurths help that kept me going during my experiments.

I would like to thank all employees and students at the Fraunhofer Center for Laser Technology for their advice and suggestions.

Thanks to my fellow student Dipl.-Ing. (FH) Manuel Kremer for many helpful discussions and his help during the writing of the thesis.

Last but not least, I would like to thank my family for their great support.

Declaration

I declare that this thesis does not incorporate without acknowledgement any material previously submitted for a degree or diploma in any university; and that to the best of my knowledge it does not contain any materials previously published or written by another person except where due reference is made in the text.

Marburg, May 18, 2005

Severin Massa

Table of contents

1 Introduction

1.1 Motivation

The next generation of fiber laser technology is being developed at the Fraunhofer Institute in Plymouth. A prototype of a high power fiber laser system of remarkable performance was built here [11][20]. The next step is to establish manufacturing processes for reproduction.

One of the advantages of the developed laser system is its modular design. It allows parts to be replaced easily for repair and upgrade. To assure a secure but easy to handle connection of the different fibers, a special plug was designed (Figure 1). For its production, two fused silica parts must be joined with a laser in a radial geometry. A disc shall be put on an end cap fiber and welded to it. It allows the both to be enclosed in a plug later on by laser brazing. The connection should be smooth on the whole circumference and must be strong enough to hold the fiber in place. The optical properties of the fiber must not be impaired during the process.

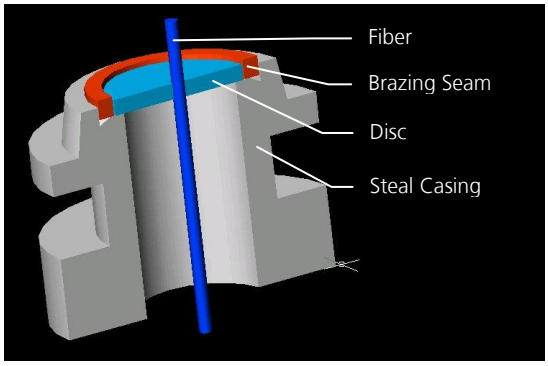

Figure 1 *Design of the fiber plug*

To develop a laser welding process, the unique properties of fused silica must be understood. Its peculiarities have to be taken account of and finally the geometry of the parts must be considered.

1.2 Disposition of the thesis

As a first important step, the properties of fused silica must be understood. Therefore, chapter 2 is devoted to the special characteristics of fused silica glass. After a first overview of the physical properties of fused silica in chapter 2.1, the structure of silica and its polymorphs as well as the synthesis of fused silica glass is described in chapter 2.2. Chapter 2.3 and 2.4 then take a closer look at viscosity and surface tension, which are important characteristics of glasses. Chapter 2.5 evaluates the properties of fused silica for laser welding processes.

Regarding the properties of fused silica mentioned in chapter 2, the actual joining process is developed in chapter 3. After describing the process conditions like equipment, material and geometry of the seam in chapters 3.1 to 3.3, the process is simulated mathematically to approximate the behavior of the glass in chapter 3.5.

The actual welding experiments are described in chapter 4. Several problems occurred during the experiments as mentioned in chapter 4.1, which lead to a changed experimental setup described in chapter 4.2.

The results of the experiments with the new setup are described in chapter 5.

Finally, a résumé of the achieved cognitions is given in chapter 6.

2 Fused silica

2.1 Properties

Laser welding of regular glasses has already been done at Fraunhofer USA [9]. Fused silica, however, has significant properties that distinguish it from traditional glass. The primary distinguishing characteristic is its purity. Pure fused silica consists exclusively of silicon dioxide (SiO_2). Only small levels (10-1000 ppm) [38] of impurities such as hydroxyl (OH) groups are introduced during the primary glass fabrication step. Thus, the level of purity is equivalent to that of semiconductor materials. In connection with its amorphous structure, a number of spectacular characteristics are accomplished.

2.1.1 Mechanical properties

The tensile strength of fused silica can reach up to 50 N/mm² [16]. In practice, however, it strongly depends on the number and concentration of surface defects, which, in combination with atmospheric influences, such as moisture, reduce the tensile strength. Furthermore, the geometry of a fused silica piece plays a role. Even the type of surface treatment and the age of fused silica influence its properties (see also chapter 2.2.2.3).

The chemical resistance of fused silica is outstanding. It is attacked by a few compounds only, one being hydrofluoric acid.

Fused silica has a density of: $\rho = 2201 \frac{kg}{m^3}$.

2.1.2 Optical properties

The optical properties of fused silica are distinguishing it from regular glasses. The transmissive wavelength range depends on the respective material but lies between 160- and 3500nm. Here, the absorption coefficient is so small as to be practically immeasurable.[15]

The absorption at the UV edge is reduced to the lifting of electrons to the conduction band. Fused silica has a band gab of about 8.5eV [5] which corresponds to a wavelength of about 145nm.

The radiation energy in the long-wave range is converted to lattice vibrations. The quantized vibrations are called phonons. Various harmonics of the vibration statuses of the SiO_4 tetrahedra can be detected from approx. 3500nm, before total absorption starts at approx. 4000nm.

While its excellent transmission makes fused silica the preferred material for optical fiber manufacturing, a high absorption is needed for welding. With total absorption above 4µm, the beam of a CO_2-laser at about 10.6µm is absorbed completely on the surface.

MCLACHLAN and MEYER [23] measured the extinction coefficient k_{ex} of fused silica at 10.6µm wavelength as 0.025. The extinction coefficient is related to the absorption coefficient as:

$$\alpha = \frac{4\pi}{\lambda} \cdot k_{ex}$$

Equation 1 *Calculation of absorption coefficient from extinction coefficient*

The absorption coefficient of fused silica at 10.6µm wavelength is then

$$\alpha = 2.96 \cdot 10^4 \, m^{-1} .$$

The absorption coefficient does not change significantly with temperature, as shown in [14][26][27][28] for smaller wavelengths.

2.1.3 Thermal properties

2.1.3.1 Working Point and temperature of vaporization

As described later, glasses have no sharp melting point like other materials. Due to their vitreous structure, bonds are breaking one after another, leading to a slow decrease of viscosity. Fused silica softens at about 1600°C and can be readily formed above about 2000°C (see chapter 2.3).

The boiling point of SiO_2 is 2230°C. Nevertheless, vitreous silica begins to pyrolyze above about 1350°C already, by the reaction: $2SiO_2 = 2SiO + O_2$ according to BANSAL [1], who speaks of

"vaporization" at these low temperatures already (see also chapter 2.2 for composition of fused silica).

The SiO is oxidized again forming SiO_2 granules on the colder glass and can be observed as a band of haze just outside the intensely heated region.

When working with fused silica, pyrolyzation cannot be avoided since temperatures above 2000°C are needed. Accumulation in the area of the beam impact leads to higher temperatures on the surface. When thermal conduction is too slow, even the boiling point may be reached, resulting in massive vaporization in this area. The experiments showed that this is unproblematic as long as the intensity on the surface is limited, allowing a smooth spreading of heat.

2.1.3.2 Thermal expansion coefficient and thermal shock resistance

One of the most outstanding properties of fused silica is its low thermal expansion coefficient of approx. $0.55 \cdot 10^{-6} K^{-1}$ between 20°C and 1000°C. This means that thermal expansion is about 20 times lower than that of normal window glass and 30 times lower than that of stainless steel. In turn, the low thermal expansion coefficient leads to an enormous thermal shock resistance. Consequently, even products at 1500°C withstand exposure to cold water without any damage [12]. In addition to the thermal expansion coefficient, however, surface condition and geometry influence thermal shock resistance.

2.1.3.3 Heat capacity

The specific heat capacity of a solid or liquid is defined as the heat required to raise a mass of substance by one degree of temperature.

According to HARPER [15], the solid-state heat capacity of most silicate glasses is about

$$c_p = 1.255 \frac{kJ}{kg \cdot K}.$$

The change in heat capacity is rather low, compared to other materials [12][34]. For later calculations, the value given by HARPER will be used.

2.1.3.4 Thermal conductivity

Heat conduction in metals is based on free electrons. In dielectric media like fused silica, only conduction thru vibrations (phonons) is possible.

According to CHONG [6], the thermal conductivity for fused silica satisfies the following relationship:

$$\lambda_{FS}(T) = 0.78 - 0.054 \cdot e^{\frac{T+379}{354}} + 0.165 \cdot e^{\frac{T+379}{405}}$$

Equation 2 *Temperature dependence of thermal conductivity with T in K.*

The propagation of thermal conductivity with temperature is shown in Figure 2.

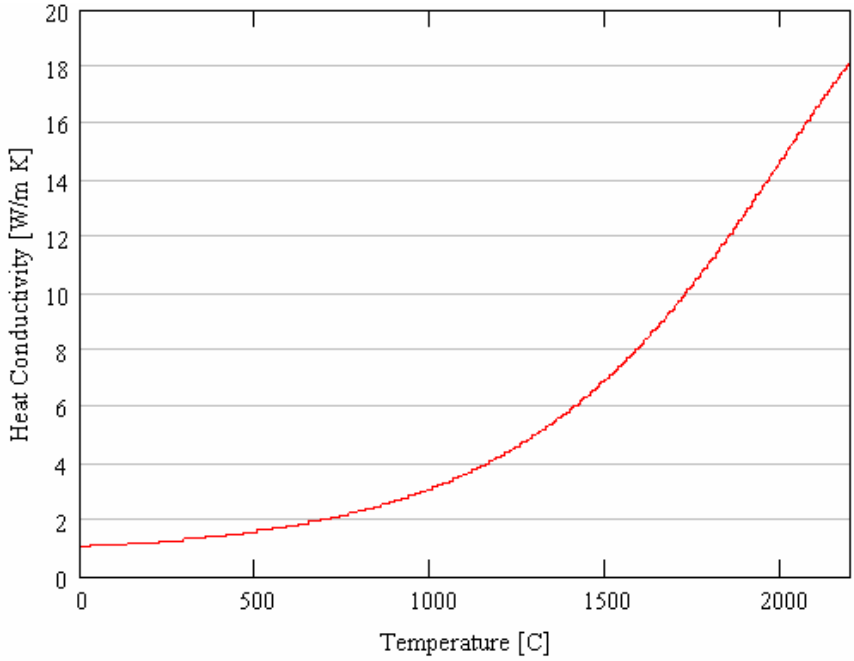

Figure 2 *Thermal conductivity in fused silica for temperatures between 0°C and 2000°C*

For some calculations, the integral mean of the thermal conductivity in a specific temperature range may be used [22]:

$$\overline{\lambda}_{FS} = \frac{1}{T_2 - T_1} \int_{T_1}^{T_2} \lambda_{FS}(T) dT$$

Equation 3 *Mean thermal conductivity for a specific temperature range*

2.2 Composition and manufacturing

2.2.1 Types of silica

Fused silica or "quartz glass" is a silicate. Its basic structural unit is the silicon-oxygen tetrahedron. Every Si is surrounded by four O, building a tetrahedron. Every O connects two Si (SiO_2). SiO_2 is a polymorphous material, meaning it can build different structures with the same formula. The most common structure is quartz, which is divided in α- and β-quartz by its crystal structure. α-quartz builds a trigonal crystal system, while β-quartz has a hexagonal crystal system. The transformation between both is reversible and happens at rather low temperatures. Figure 3 shows a three dimensional view of the atomic structure of α-quartz.

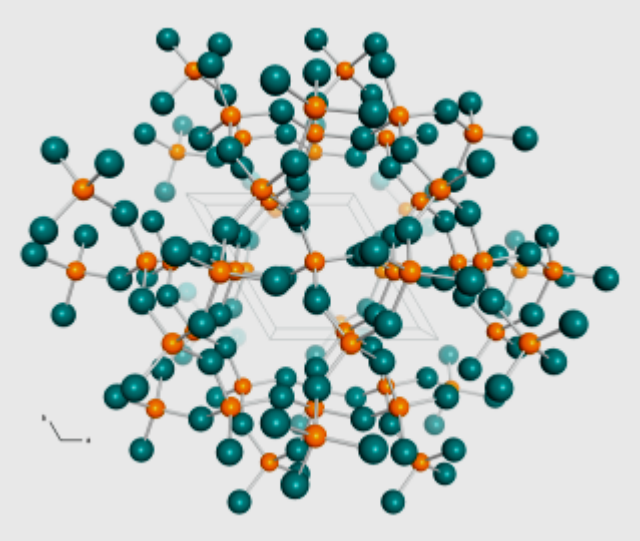

Figure 3: *Perspective view of the crystal structure of α-quartz (DIAMOND drawing [4]) based on parameters taken from the ICSD data base [18]. [• =Si, • =O]*

α-Quartz is the stable form of SiO_2 at temperatures below 870°C. High temperature polymorphic forms are Tridymite and Cristobalite the formation of which requires breaking up and forming new bonds. Owing to the high activation energy for such processes, these modifications can be obtained as metastable forms at ambient conditions. The same holds

for silica in its glassy form, interesting here. As shown in Table 1, Quartz, Tridymite, and Cristobalite all occur in an α- and a β-form that differ in slight rotations of the [SiO_4] tetrahedron relative to one another only and can transform easily, therefore. When these three polymorphs form at the appropriate temperature, they first show the β-modification (see Figure 4). When they cool below a particular temperature (specific for each form), they transform into the α–form, stable at normal temperature. [15]

Other silica polymorphs occur under extreme conditions only and are of no interest to this paper. Coesite and Stishovite form under very high pressure only. Lechatelierite is a very rare, amorphous form of silica, which is considered a glass. Keatite is synthetic silica that does not appear in nature. [10]

Table 1 lists all forms of silica with the corresponding crystal system and class.

Polymorph	Crystal System	Crystal Class
α-Quartz	trigonal	3 2
α-Tridymite	various complex orthorhombic or monoclinic variants	$\frac{2}{m}\frac{2}{m}\frac{2}{m}$ *or* $\frac{2}{m}$
α-Cristobalite	tetragonal	4 2 2
β-Quartz	hexagonal	6 2 2
β-Tridymite	hexagonal	$\frac{6}{m}\frac{2}{m}\frac{2}{m}$
β-Cristobalite	cubic	$\frac{4}{m}\bar{3}\frac{2}{m}$
Coesite	monoclinic	$\frac{2}{m}$
Stishovite	tetragonal	$\frac{4}{m}\frac{2}{m}\frac{2}{m}$
Lechatelierite	amorphous	---
Keatite	tetragonal	4 2 2

Table 1 *Different polymorphs of silica [10]*

Figure 4 shows a p-T phase diagram for the most common silica forms. As mentioned above, the different types can convert into each other. The thermodynamically preferred structure for given conditions is called stable. There are transformation points marked in Figure 4, showing the temperature at which one structure usually changes to another.

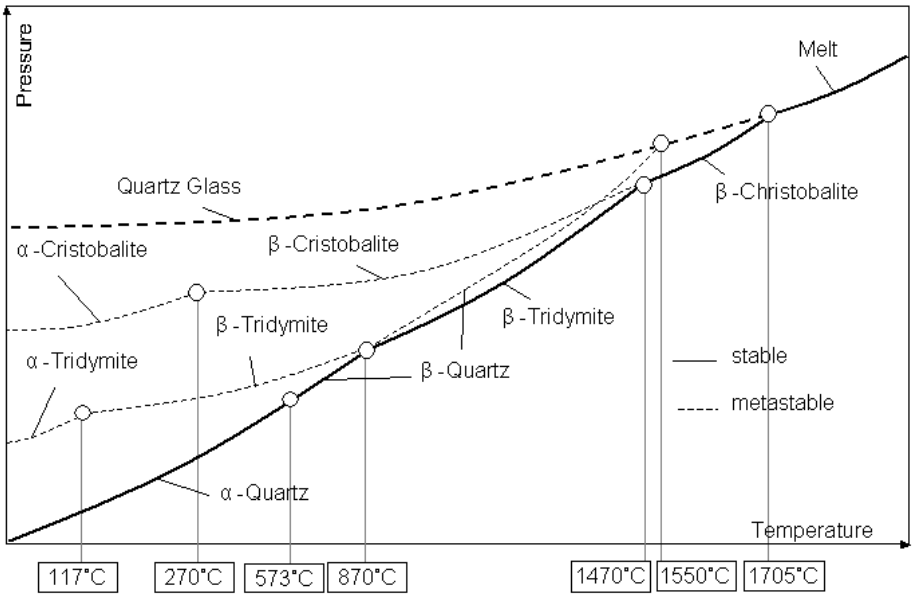

Figure 4: *SiO_2 p-T Phase Diagram [37]*

2.2.2 Synthesis of fused silica glass

Fused silica is made of melted quartz by cooling it down fast from temperatures above about 1705°C. This is the melting temperature of β-cristobalite. Above this temperature, no crystallization occurs under normal conditions (atmospheric pressure) but the melt still has a high viscosity (see chapter 2.3). When cooling down fast, the covalently bonded SiO_2 cannot rearrange into the thermodynamically stable crystal structure. The [SiO_4] tetrahedra connect in a random network with no long-range order. This is called a vitreous state. Although, it is not the thermodynamically preferred structure, fused silica glass shows high kinetical stability.

2.2.2.1 Glass transition

There is no sharp distinction between the liquid and the glass state like there is between the liquid and the solid state. The latter transforms by a first order phase transition meaning a discontinuous change in the properties of the material such as density. Because the second-derivative thermodynamic properties such as heat capacity, thermal expansion coefficient, and isothermal compressibility display steep changes in fused silica at a specific transition range, it is sometimes referred to as a second order transition [13]. In fact, it is generally agreed that it is not a second-

order thermodynamic transition. According to HARPER [15], it is best referred to as a "freezing-in" transition.

The temperature range at which the glass transition takes place in fused silica is at around 1200°C [13]. It depends on the cooling rate. Slow cooling allows the material to relax and the transition occurs at a lower temperature. The glass is then denser. If cooled too slowly, however, the material can crystallize. This so-called devitrification is described in chapter 2.2.2.3.

2.2.2.2 Vitreous state

The disordered glassy state does not have enough kinetic energy to overcome the potential energy barriers required for rearrangement of the [SiO_4] units, preventing a long-range order. No equal bond strengths exist and therefore, when heated up again, the bonds break up one after another, leading to the typical behavior of glass.

In Figure 5, the vitreous state of quartz (fused silica) is compared to the crystalline state (α-quartz). For simplification, the schematic structures are shown in 2D, where one O of each SiO_4 tetrahedron is not shown.

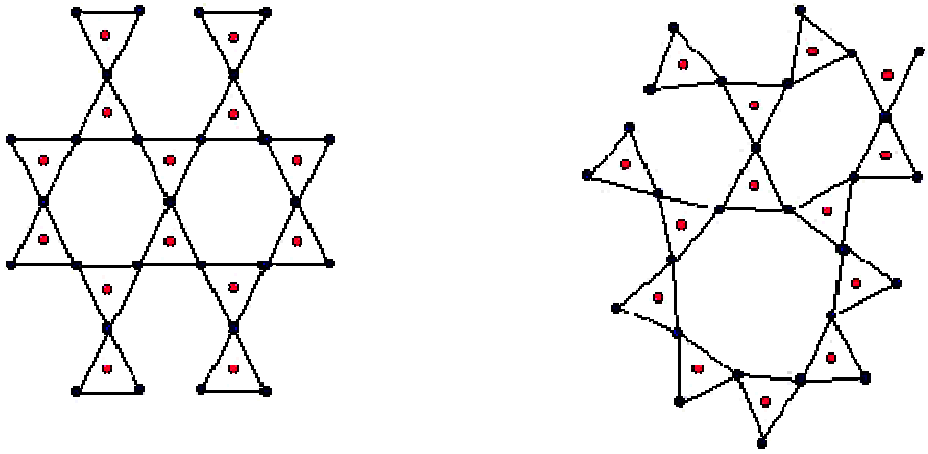

Figure 5 *2D-view of crystalline SiO_2 (α-quartz) (left) and fused silica glass (right). In vitreous state, the [SiO_4] tetrahedral are disordered, lacking a long-range order. [• = O, • = Si] [15]*

2.2.2.3 Cooling rate and devitrification

Generally, any substance (even metal) may be brought to glassy state provided that its melt is cooled at a rate fast enough to prevent rearrangement in a crystal structure. The minimum cooling rate needed

for this is called critical cooling rate. When cooling too slowly, crystallization may occur. Since the glass is changing from its vitreous state to a crystalline state, this process is called devitrification.

Devitrification must be avoided at any cost, since it can damage the material severely. It usually starts on the surface, from where it penetrates further into the material. The penetration speed is an exponential function of temperature. In the devitrification process, a crystalline material forms whose structure corresponds to β-cristobalite. As the density is virtually identical, the β-cristobalite layer on the fused silica cannot be discerned visually. At 270°C, however, the crystal structure turns from β-cristobalite into α-cristobalite, which is accompanied by a strong reduction in density. The material may then crack or break, visible on the surface by white spots. The tetragonal α-cristobalite structure exhibits a refractive index, which greatly differs from that of fused silica. [1]

To avoid devitrification, nucleation must be limited. Any contamination of the material must be avoided. A high vapor pressure or chloride addition likewise accelerates the process. Consequently, the rate of devitrification of fused silica increases with increasing hydroxyl (OH)- content, decreasing viscosity and increasing temperature. Handling of fused silica with bare hands deposits sufficient alkali from perspiration to leave clearly defined fingerprints upon devitrification [12]. For more information about devitrification in optical fibers, also see the work of ROSE [32].

Devitrification is a two-step process of nucleation and growth. Since fused silica is a high purity material, nucleation is generally initiated by surface contamination. Particularly the alkali metals sodium or potassium act as electron donators and destroy the cross-linked silicon-oxygen structure, triggering devitrification. The necessity of breaking and reforming Si–O bonds explains the low growth rate of only $2.18 \cdot 10^{-7}$ at 1754°C (less at lower temperatures) given by BANSAL [1]. Nucleation and crystallization rates are exponential functions of temperature. [32][33][35]

As shown by HARPER [15], a curve can be constructed by computing the time needed to develop an experimentally discernible amount of crystals (typically 1ppm) in a melted mass in which the nucleation- and crystal growth rates are known.

Figure 6 shows such a typical time-temperature transformation (T-T-T) diagram for glass formation.

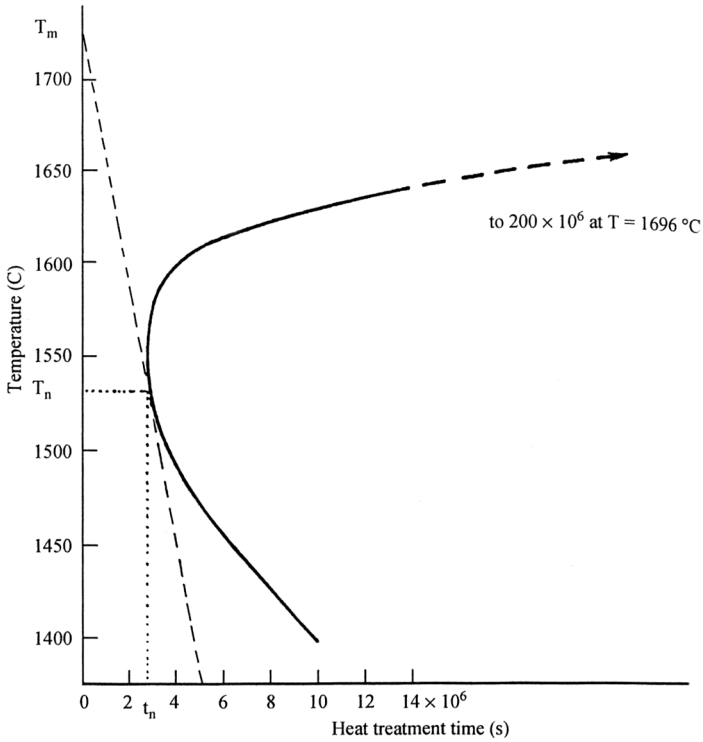

Figure 6 *A typical time-temperature-transformation (T-T-T) diagram for glass formation after UHLMANN [36]*

When T_m is the temperature of the melt, the critical cooling rate is the line drawn sloping downward from T_m that is tangent to the nose. The temperature where the line intersects the nose is called T_n. As long as cooling is fast enough, the line stays to the left of the nose and perceptible crystallization may not develop.

The critical cooling rate is calculated as $(T_m - T_n)/t_n$, where t_n is the time corresponding to T_n. Its unit is then K/s. Table 2 gives some examples of critical cooling rates.

Material	Homogenous nucleation [K/s]	Hetrogenous nucleation contact angle [K/s]		
		100	60	40
SiO_2 glass	$9 \cdot 10^{-6}$	10^{-5}	$8 \cdot 10^{-3}$	$2 \cdot 10^{-1}$
GeO_2 glass	$3 \cdot 10^{-3}$	$3 \cdot 10^{3}$	1	20
$Na_2O \cdot 2SiO_2$ glass	$6 \cdot 10^{-3}$	$8 \cdot 10^{-3}$	10	$3 \cdot 10^{2}$
Salol	10			
Water	10^{7}			
Ag	10^{10}			
Typical metal	$9 \cdot 10^{8}$	$9 \cdot 10^{9}$	10^{10}	$5 \cdot 10^{10}$

Table 2 *Examples of critical cooling rates for glass formation after ONORATO, P.I.K. AND UHLMANN, D.R. [30]*

Allowing cooling rates of as low as $9 \cdot 10^{-6}\ K/s$, SiO_2 can be brought to glassy state easily. This results from its high purity and the low growth rate. As shown in chapter 3.5.5, when calculating the temperature in fused silica, a small mass of fused silica cools down fast enough on its own to avoid devitrification. No further cooling is required.

2.2.3 Weathering

Besides losses through devitrification, ROSE [32] also observed OH absorption in optical fibers. OH enters the fiber through a reaction with water from the air and oxygen in the glass. Increased absorption due to OH was measurable after annealing for 17 hours. It should therefore not be a problem for the short process times used. When stored on air unprotected, however, this process can slowly destroy the fiber even at room temperature. As a general rule, only small pieces of fiber should be stripped to avoid unnecessary exposure to the environment.

2.2.4 Regular glasses

In regular glasses (window glass), the addition of alkaline bases like Na_2O or CaO leads to an increased breaking up of the structure. Some of the additional oxygen cannot connect to another $[SiO_4]$ tetrahedron. Integrating Na^+-ions into the cavities compensates the resulting charge. This leads to a lower viscosity and thus a significantly lower softening point. The amounts of additives allow the physical properties of the glass to be adjusted in a wide range. The 2D-structure of regular (window-) glass is shown schematically in Figure 7.

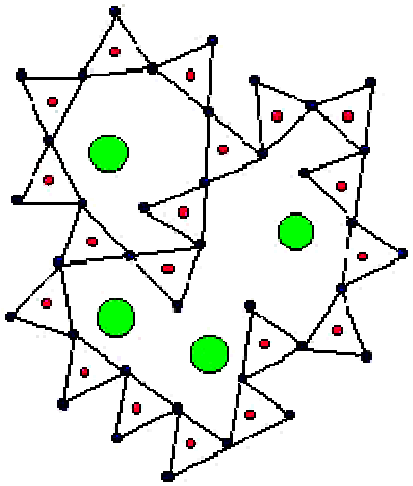

Figure 7: *2D-structural scheme of regular window glass. [• = O, • = Si, ● = Na] [15]*

2.3 Viscosity

2.3.1 Definition of viscosity measurands according to DIN ISO 7884

The dynamical viscosity coefficient η is defined in the DIN ISO 7884 [8] as the force *F*, needed to displace two parallel areas *A* distant to each other by Δx, with the relative speed Δv.

$$\eta = \frac{F \cdot \Delta x}{A \cdot \Delta v}.$$

Its SI unit is $Pa \cdot s$ or $\frac{N \cdot s}{m^2}$. However, the unit Poise (P) is still used, where 1 $Pa \cdot s$ equals 10 P.

2.3.2 Viscosity of glasses

Viscosity is the most important physical property of glass for industrial reproduction. The characteristic temperatures of glass are defined thru viscosity and it is of great importance to this experiment to describe the behavior of the melted glass.

The viscosity of glass spans from about 10^2P (melt) to 10^{22}P (room temperature). 10^2P is about the viscosity of hot molasses [15] while water at room temperature has a viscosity of only 10^{-2}P. The high viscosity fused silica glass has even at high temperature is due primarily to the high tetrahedral connectivity of the network.

Practically, three viscosity regions are differed.

- Melted Range: up to 10^3P
- Working Range: 10^3 to 10^8P
- Freezing Range: 10^{13} to 10^{15}P

Four temperatures are usually given to define the viscosity-temperature behavior of a material:

- Working Point ϑ_{f1}
  Viscosity: 10^4 P
  At the working point, the glass can be readily formed or sealed. This is the temperature needed for welding.

- Softening Point ϑ_{f2}
  Viscosity: $10^{7.6}$ P
  At this viscosity, a rod about 24cm long and 0.7mm in diameter elongates 1mm/min under its own weight.

- Annealing Temperature ϑ_{f3}
  Viscosity: $10^{13.2}$ P
  At the annealing temperature, a rapidly cooled glass becomes reasonably strain-free in about 15 minutes.

- Strain Point ϑ_{f4}
  Viscosity: $10^{14.7}$ P
  At this temperature, stresses that form in the glass object are relieved in a matter of hours.

The working point should be reached for the welding experiments. It is defined thru its viscosity. In the next chapter, the viscosity of fused silica is described.

2.3.3 Viscosity of fused silica

Like all glasses, fused silica exhibits an inversely proportional, exponential temperature dependence of viscosity [16]. Up to its strain temperature at 1000°C, the material can be regarded as a true solid. From that temperature on, fused silica starts to flow slowly. At its softening at approximately 1600°C, fused silica is still highly viscous. For welding, viscosities in the working- or even melted range might be necessary, demanding temperatures of far above 2000°C. Figure 8 shows the viscosity of fused silica with temperature as provided by GE [12]. It differs slightly from the values given by HARPER [15] (Annealing point (10^{13}P): 1130°C; softening point ($10^{7.65}$P): 1550°C) and BANSAL [1] (annealing point (10^{13}P): 1190°C; softening point ($10^{7.6}$P): 1670°C).

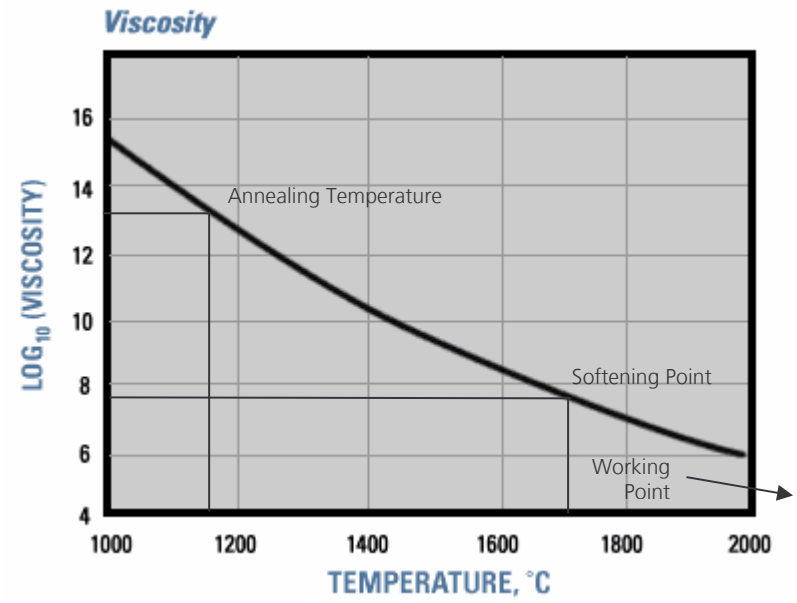

Figure 8 *Representative viscosity of fused quartz [12]*

The reason for the differences between the viscosity points of the different sources is most likely the amount of impurities in the measured glasses. Impurities have a great influence on viscosity. The hydroxyl content as well as traces of alkali and halogen, such as sodium and chloride, reduce the viscosity, whereas small concentrations of aluminum or high melting metals, such as molybdenum, have the reverse effect [16].

2.4 Surface tension

Surface tension will proof to be an important aspect during this work. It shall therefore be explained here.

The cohesive forces between molecules down into a liquid are shared with all neighboring atoms. Those on the surface have no neighboring atoms above and exhibit stronger attractive forces upon their nearest neighbors on the surface. This enhancement of the intermolecular attractive forces at the surface is called surface tension. It is shown in Figure 8.

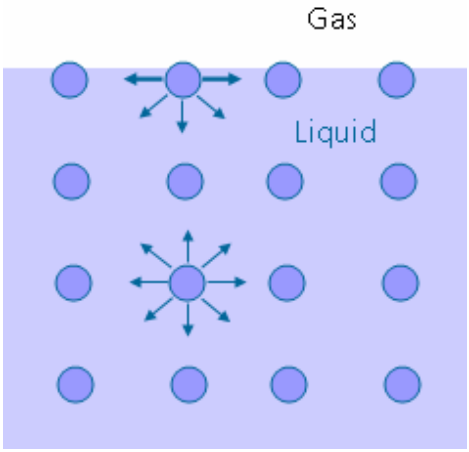

Figure 9 *Enhancement of the intermolecular attractive forces at the surface leading to surface tension. [17]*

The surface tension is the reason why drops of water usually have a spherical shape. This is described in the YOUNG-LAPLACE equation for non-spherical surfaces:

$$p_i = \sigma_T \cdot \left(\frac{1}{r_1} + \frac{1}{r_2} \right)$$

Equation 4 YOUNG-LAPLACE *equation for non-spherical surfaces*

where p_i is the internal pressure caused by the surface tension σ_T and r_1 and r_2 are the main radii of curvature. The internal pressure rises with decreasing radii of curvature. Therefore, a liquid always strives for

maximum radii and in the end a spherical shape. Then r_1 and r_2 are equal, leading to the spherical YOUNG-LAPLACE-equation:

$$p_i = \frac{2\sigma_T}{r}.$$

Equation 5 YOUNG-LAPLACE *equation for spherical surfaces*

Surface tension changes with temperature. In general, surface tension decreases with raising temperature and is 0 when the liquid reaches its boiling point. For pure silica melts at 1200°C, HARPER [15] lists a surface tension of 280mN/m. It decreases by 4 to 10 mN/m per 100K increase in temperature. Extrapolating this, fused silica at 2000°C would still have a rather high surface tension. OLSEN and OSTERAAS [29] report that the surface tension of all types of glass melts is nearly the same as that of water [25]. Water at room temperature has a surface tension of 72.75mN/m.

With its relatively high surface tension, liquid glass will strongly strive for a minimization of surface area and radii of curvature. In a welding experiment, this can lead to a withdrawing of the material if no connection is established. However, once a connection is established, surface tension has the opposite effect, leading to attraction between the parts, now trying to minimize the common surface area (see chapter 4.1.4).

2.5 Relevance of the physical properties of fused silica for laser welding processes

As mentioned in chapter 2.1.2, total absorption occurs above approximately 4000 nm. A CO_2-laserbeam at about 10600nm is therefore absorbed at the surface completely.

The thermal data of fused silica seem to be perfect conditions for a welding process. The very low coefficient of thermal expansion, which leads to the mentioned thermal shock resistance prevents tension or cracks in the material. Devitrification should not be a problem for the experiments, as well. As shown later in the calculations (chapter 3.5), the cooling rate is high enough to avoid devitrification. Nevertheless, contamination of the material must be avoided. It will later show, that a number of problems occur during the process. When looking at the thermal properties of fused silica, some of them can already be predicted.

The thermal conductivity of fused silica rises steeply with temperature. At low temperatures it is rather low compared to that of steel. When trying to use a regular laser welding process with plasma capillary, this causes a much steeper temperature gradient of the plasma capillary due to the lack of heat conduction and leads to massive vaporization because of the low boiling point. In the end, the glass is cut more then melted. As a result, a plasma capillary cannot be used in glass. The energy of the laser can therefore only affect the glass surface and must spread thru thermal conduction. Additionally, the radial geometry of the seam demands the heat to flow to the actual seam, as shown in chapter 3.3.

With pyrolyzation occurring at rather low temperatures, it cannot be avoided but must be reduced by limiting intensity on the glass. The energy should be spread evenly over the whole seam to allow a slow heating up of the whole setup. The temperature should then be held at a value enabling the glass to flow but below the boiling point of 2230°C. The ability of the laser to deliver very precise amounts of energy makes it the optimal tool for this task. By using a fast scanning process with low intensity, the energy can be spread evenly.

Surface tension in connection with the geometry of the seam proofed to be a big problem for the process. The radial seam and the unavoidable gap between fiber and disc (see chapter 3.3) are problematic. Since liquid glass has a surface tension similar to that of water, it strives to minimize

radii and surface area just like water does. Its preferred shape is spherical, leading to a withdrawing of liquid material.

The following chapters describe the approach to the development of the process. The problems mentioned above were discovered during the simulation and experimenting and are described in chapter 4.1.

3 Development of joining process

3.1 Equipment

3.1.1 Laser

A Rofin Sinar SCx10 pulsed 100W CO_2 laser is used. It has a fixed pulse power of 200W. Only varying pulse period (PP) and pulse width (PW) controls the average power. Since it allows duty cycles ($DC = PW/PP$) of up to 50%, its average power reaches 100W.

Table 3 lists the most important properties of the used laser.

Property	Symbol	Value
Max. Average Output Power	P_{AV}	100 W
Pulse Power	P_L	200W
Power Stability	ΔP_{AV}	± 7%
Beam Propagation Factor	K	>0.8
Beam Divergence	θ_0	<2.5 mrad (full angle)
Beam Diameter (1/e^2)	d_L	7.5 ± 0.5 mm
Wavelength	λ	10.4 – 11.2 µm

Table 3 *Properties of the laser beam given in the operating manual [31].*

The average output power of the laser is not linear with set duty cycles. It was measured and a third order polynomial fit is used to calculate it:

$$P_{AV}(DC) = -0.0001 \cdot DC^3 + 0.0039 \cdot DC^2 + 0.3897 \cdot DC - 2.9376$$

Equation 6 *Polynomial fit to calculate average laser power from duty cycle*

The laser-scanner distance (LS) is 1150mm. With the given divergence (θ), the raw beam diameter at the scanner (d_R) can be calculated as follows:

$$d_R = d_L + \theta \cdot LS \qquad d_r = 11.4mm$$

The scanner lens has a focal length (f) of 100mm. This allows some beam parameters to be calculated: [2][3]

- Wavenumber

$$k = \frac{2\pi}{\lambda} \qquad k = 593mm^{-1}$$

- Divergence of focused beam (full angle)

$$\theta_F = \frac{d_r}{f} \qquad \theta_F = 0.114$$

Equation 7 *Divergence of a focused beam*

- Focus Diameter (1/e^2)

$$d_0 = \frac{\lambda}{\pi}\frac{4}{\theta_F}\frac{1}{K} \qquad d_F = 148\mu m$$

Equation 8 *Beam diameter in focus*

- Rayleigh Length

$$z_R = \frac{\pi \cdot \left(\frac{d_0}{2}\right)^2}{\lambda} \qquad z_R = 1.3mm$$

Equation 9 *Rayleigh Length*

The laser has a beam propagation factor K of 0.8. The beam propagation factor defines the similarity of the beam profile to a Gaussian profile. For example, the lower beam propagation factor leads to a bigger focus

diameter compared to the idealized Gaussian beam. This must be considered when calculation the beam properties. Figure 10 shows a schematic view of an idealized Gaussian profile.

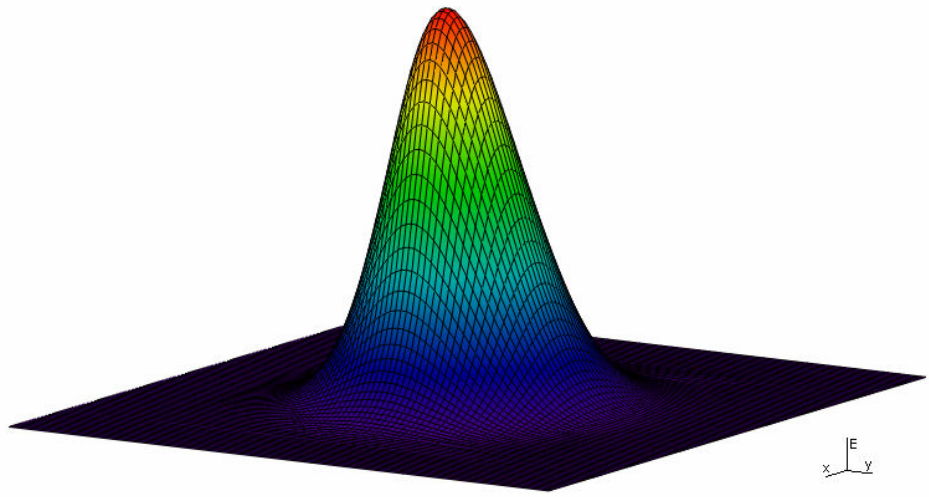

Figure 10 *Schematic view of an electrical field strength profile with gauss shape.*

Here, the transverse profile of the electric field strength of the beam can be described with a Gaussian function:

$$E(r,z) = E_0 \cdot \frac{1}{\sqrt{1+\left(\frac{z}{z_R}\right)^2}} \cdot \exp\left\{-\frac{k \cdot r^2}{2z_R}\frac{1}{1+\left(\frac{z}{z_R}\right)^2}\right\}$$

Equation 10 *Gaussian function of the transverse electric field strength profile. [3]*

where E_0 is the amplitude of the electrical field strength, z_R is the Rayleigh length and k is the wavenumber as described above.

Using the beam properties calculated above, the distribution of electric field strength can be calculated for every z-position and radius. In Figure 11, the progression of the electric field strength relative to its maximum amplitude in focus ($z = 0$) is shown. 4mm from the focus, the radial distribution is already much shallower than in focus. Concordantly, the beam diameter is bigger.

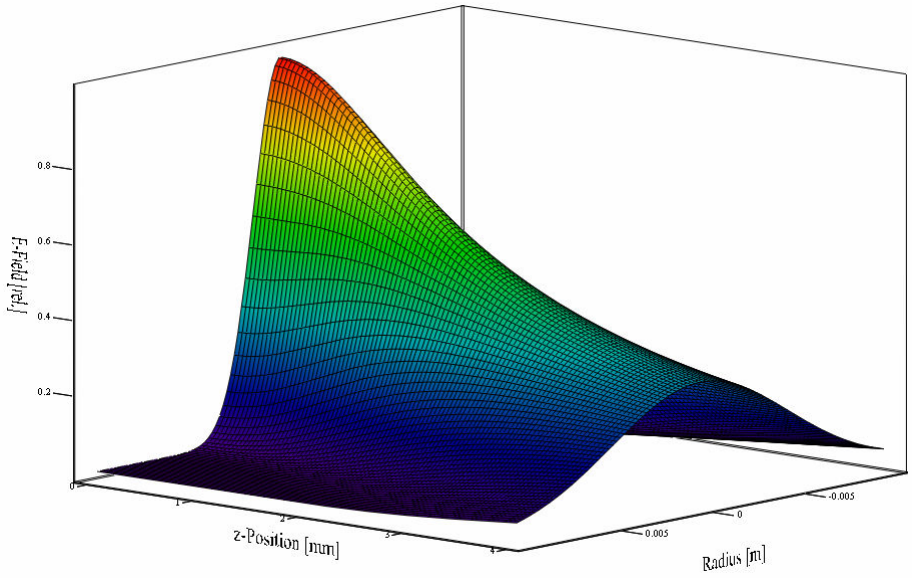

Figure 11 *Progression of relative electric field strength of the laser beam.*

The beam diameter $d(z)$ (twice the distance from the beam axis where the intensity drops to $1/e^2$ (about 13.5%) of the maximum value) can be calculated as follows:

$$d(z) = d_0 \cdot \sqrt{1 + \left(\frac{z}{z_R}\right)^2}$$

Equation 11 *Beam diameter for z-position*

The beam radius ($d(z)/2$) is shown in Figure 12. The radius increases linear in far field approximation (Fraunhofer region: $z >> z_R$) and takes on a hyperbolic shape near the focus. The beam has a Rayleigh length of 1.3mm and a closer look at the focus region shows that this is about the distance from which on the radius increases linear.

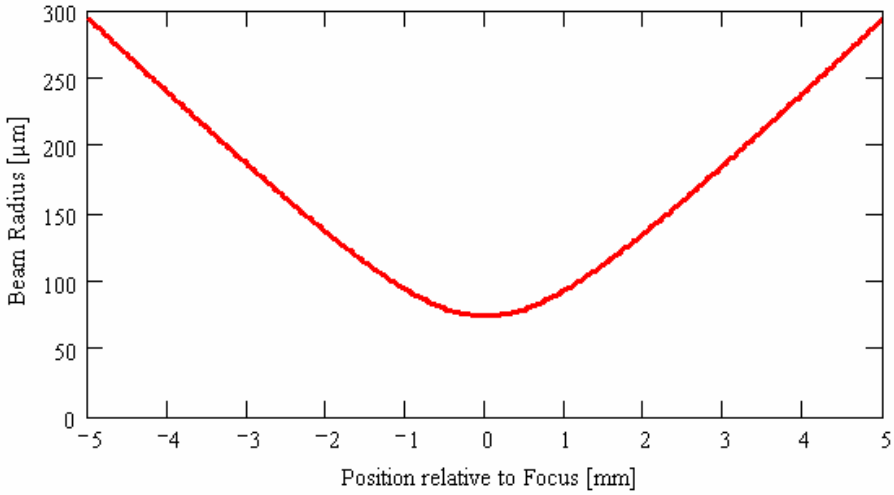

Figure 12 *Calculated beam radius at positions relative to the focus from -5mm to +5mm.*

Intensity on the glass must be limited as mentioned in chapter 2.1.3.1. It is defined as the power in a certain area. For this setup, the intensity is the Pulse Power in the spot area on the surface.

$$I_S = \frac{P_L}{\pi \cdot (d_S/2)^2}$$

Equation 12 *Intensity on the surface*

With a fixed pulse power a larger beam spot is needed to decrease intensity. However, a small focus is evident for the process to minimize circle diameter without damaging the fiber. To allow smaller focuses with low intensity, a partly reflector is used, reducing laser power by 80%. Thru this, the pulse power (P_L) is limited to 64W (calculated from measurement of average power) and lower focus positions are possible. The beam must still be defocused by at least $z_F = +4mm$, leading to a beam diameter on the surface of $d_S = 480\mu m$.

The pulse period should be minimized to achieve good pulse overlap and to avoid cooling down of the glass between the pulses (see chapter 3.5.3). With short pulse periods, the setting of pulse width, and therefore average power becomes inaccurate. A pulse period of 200µs proofed to be a good compromise. Further settings are described later.

3.1.2 Scanner system

A scanning optic allows fast traverse speeds. Thru this, energy is spread evenly over the whole seam. Increasing number of scans raises the total energy induced. The necessity of high traverse speeds makes the use of a rotary axis impossible. With high rotation speed, the melted glass would flow in radial direction due to the centrifugal force.

In general, the scanning speed (v_s) should be maximized to allow the energy to spread evenly over the whole scanned circle. Meanwhile, with limited pulse period, a sufficient pulse overlap should be provided. For example, a scanning speed of $v_s = 455\,mm/s$ in combination with a pulse period of 200µs leads to a pulse overlap of 44% beam diameter. Figure 13 illustrates this definition of pulse overlap.

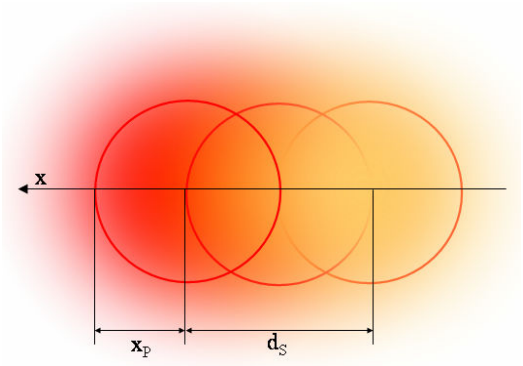

Figure 13 *Illustration of pulse overlap. Here, the overlap x_P of two pulses is about 50% of the beam diameter on the surface d_S.*

3.1.3 Fixture

A fixture was designed to clamp the fiber and hold the disc. The design is shown in Figure 14. The disc lies on an aluminum bearing table. A fine positioning table on the fixture is used to lower the disc on the fiber. Then, using a microscope, the length of fiber over the disc surface can be adjusted while the disc is held in place by vacuum. To prevent high losses thru heat conduction, the aluminum table has a center hole of 3mm diameter. The heat lost thru the contact area must still be considered for the temperature calculations. The whole fixture is positioned on a z-table with the fiber axis below the scanner. The z-table allows the relative focus position z_F to be adjusted.

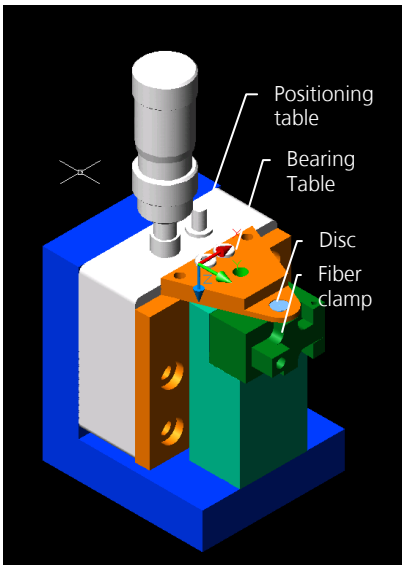

Figure 14 *Design of the used fixture*

It proofed difficult, to clamp the fiber reproducibly in the fixture especially when it is clamped with coating. This, however, is necessary to prevent weathering of the fiber. As a result, the offset of the scanned circle (see chapter 3.3) must be adjusted for every experiment. Unfortunately, no aiming optic could be used. Therefore, the scanned circle is often off, impairing results.

3.2 Material

3.2.1 End Cap Fiber

The end cap fiber (fiber) consists of pure fused silica to allow a beam to broaden inside. Spliced to the end of an active fiber, the broadened beam has a lower intensity when exiting the end cap. By this damage to the fiber end is avoided.

The fiber has a diameter of: $d_F = 400\mu m \pm 12\mu m$

The mode quality of the fiber must not be impaired during the process. Furthermore, the fiber end was planned to be already polished, ready for use. Therefore, it was a process requirement, that the fiber end is not damaged during welding. The latter had to be changed as mentioned in chapter 4.2.

3.2.2 Disc

To achieve a good connection, the disc, like the fiber, consists of fused silica. With the disc having the same thermal characteristics, the process is easier to control. Tension or cracks between end cap and disc are unlikely to occur.

The disc has a precise hole in the middle to fit on the fiber with low tolerance. It is imposed on the fiber and then welded to it. The setup with measures is shown in Figure 15.

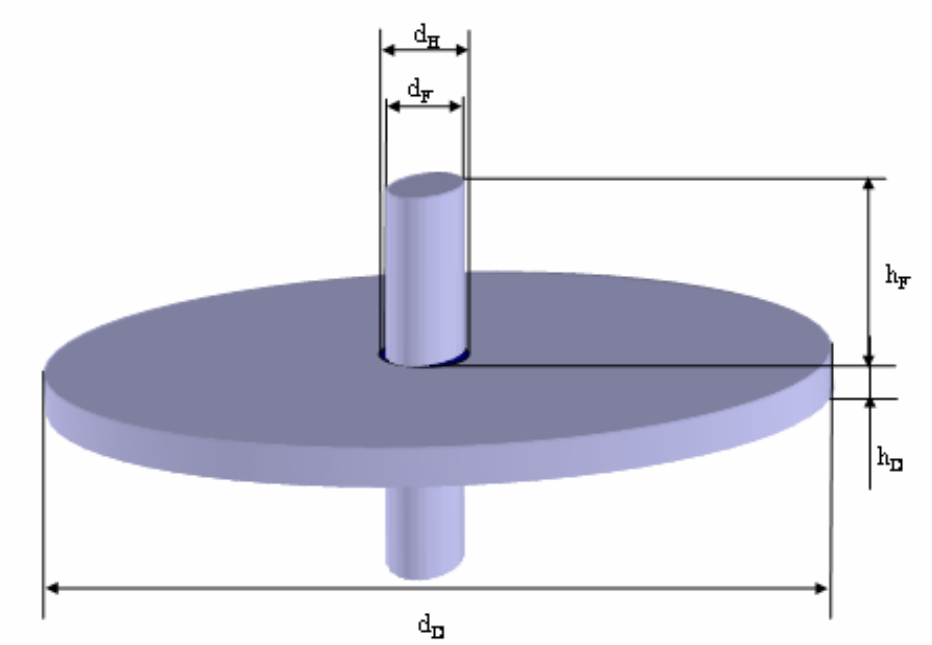

Figure 15 *Design of fiber-disc connection*

Originally, the discs thickness h_D was 300µm but, as shown in chapter 4.1.3, reaching a sufficient penetration depth during the experiments was problematic. It was therefore decided to reduce disc thickness to 150µm.

Measures of the disc:

- Thickness of the disc: $h_D = 150\mu m$
- Disc diameter: $d_D = 4.6mm$
- Hole diameter: $d_H = 0.405mm$
- Tolerance of hole diameter: $+0.01mm\,,\ -0mm$

3.3 Geometry of the seam

Disc and fiber are placed centric below the scanning optic. Therefore, the beam surrounds the fiber but can never reach the groove. Figure 16 shows the schematic process.

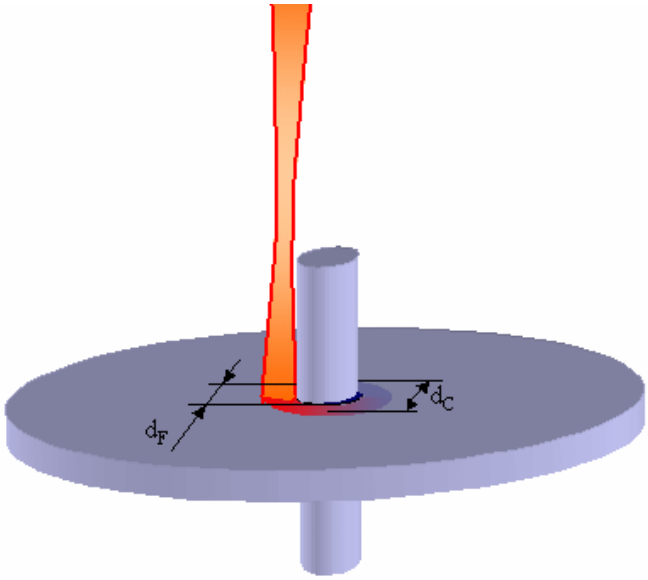

Figure 16 *Geometry of seam on disc. Laser beam hits angularly and surrounds the fiber. Welding in the groove is not possible.*

As mentioned earlier, even the attenuated beam should be defocused by $z_F = +4mm$. Experiments showed that it makes no difference whether the focus lies above or beneath the surface. A focus position above the disc is chosen to be able to draw a narrow circle without damaging the fiber end. The minimum circle diameter then depends on the length of fiber above the disc h_F, since the beam should not touch the fiber end. For example, with a fiber length of $h_F = 2mm$ and a focus position of $z_F = +4mm$, the circle diameter d_C drawn on the disc must be at least 680µm not to hit the fiber end. Figure 17 illustrates this.

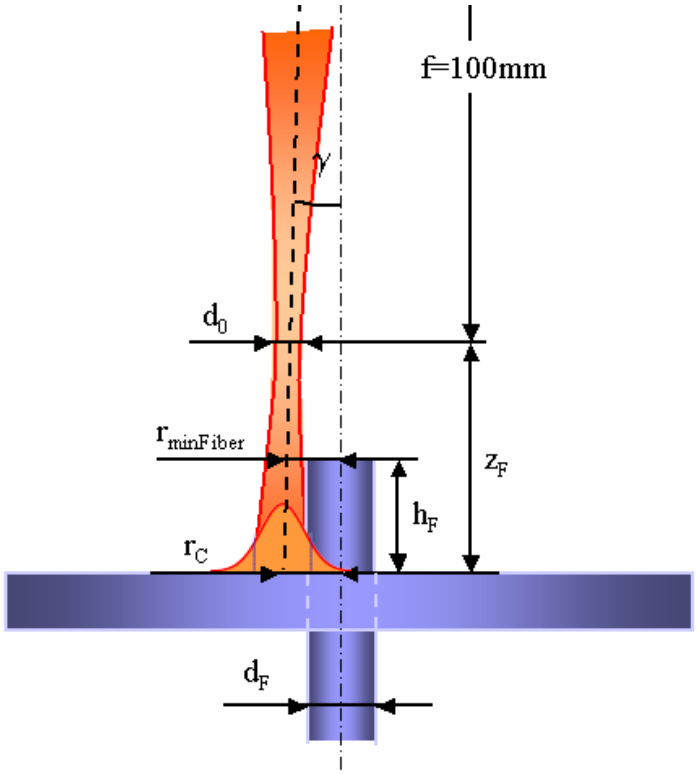

Figure 17 *Laser beam hitting the disc angularly. Beam Profile on the Disc. Part of the beam touches the fiber.*

The beam diameter (1/e²) on the disc surface for $z_F = +4mm$ is 480µm. Since the fiber diameter is 400µm, when using a circle diameter of 680µm, parts of the beam even hit the fiber. This may support the process but it must be considered, that the radial energy of the beam has the shape of a gauss distribution. Therefore, the energy hitting the fiber is only a small percentage of the total energy induced. This can be seen in Figure 17, where the beam profile is shown on the disc.

While Figure 17 shows the minimum circle diameter, a bigger circle diameter allows higher tolerances for positioning. During the experiments, the following circle diameter was determined to be practicable: $d_C = 0.8mm$.

It is obvious, that the process is based on thermal conduction, with the beam center about 200µm away from the edge of the hole. The heat must be given enough time to cross this distance and to melt the material of the disc at the edge as well as parts of the fiber. As shown in the

calculations, heat conduction in the disc is fast enough to allow low process times but the high losses are problematic and to reach the fiber, the heat has to transcend the gap between disc and fiber. This is done in part by conduction where disc and fiber have contact but mostly, the heat transfer to the fiber is based on radiation and convection. Radiation increases with temperature in the fourth potency but the radiating area is small. As a result, it is impossible to melt the fiber without establishing a connection. This is shown in chapter 3.5.2, where different types of heat transfer are compared.

It is obvious, that the biggest problem of the chosen radial geometry is the gap between fiber and disc. Although, the fiber, as well as the disc has very low tolerances, a gap between both cannot be avoided. The tolerances given by the manufacturers of disc and fiber add up to 27µm, which is the maximum width of the gap on one side, when fiber and disc have contact on the other.

3.4 Parameter settings

During the experiments, it was decided to lower the thickness of the disc from 300µm to 150µm (see chapter 4.1.3). This allows reducing process time dramatically. The parameters used for the calculation are already the parameters for the thinner discs.

The following settings led to good results during the experiments and will be used for the calculations:

Parameter	Setting
Pulse Period	$PP = 200\mu s$
Pulse Width	$PW = 23\mu s$
Duty Cicle	$DC = \frac{PW}{PP} = 11.5\%$
Average Laser Power	$P_{AV} = 7.2W \pm 0.5W$
Pulse Energy	$E_P = P_L \cdot PW = 1.47mJ$
Focus position	$z_F = +4mm$
Beam diameter on surface	$d_S = 480\mu m$
Intensity on Surface	$I_S = 2515W/mm^2$
Scanning Speed	$v_s = 455mm/s$
Pulse Overlap	44%
Length of Fiber	$h_F = 2mm$
Scanned Circle Diameter	$d_C = 0.8mm$

Number of Scans	1000
Total Process time	$t_p = 14s$

Table 4 *Experimentally determined parameters for the described experimental setup with the 150µm disc.*

3.5 Simulation of welding process

3.5.1 Goal of the simulation

Not only can the simulation of a process help finding the right parameters but also is it possible to proof discoveries made during experiments. Both is tried to achieve with these calculations.

At first some calculations are made to confirm experimentally determined settings for the welding experiments like pulse period and laser power.

Some problems occurred during the experiments, as mentioned in chapter 4.1. For example a sufficient penetration depth could not be reached with the 300µm disc. It was believed, that these problems are a result of bad heat conduction but even increasing the total process time to far above one minute did not improve results.

Finite element methods (FEM) would be necessary to simulate heat flow in complex geometries like the disc. The laser only heats the surface of the disc while thermal conduction spreads the heat in the disc. For a rough approximation of the heat flow, however, another method may be chosen. The heat flow in the disc is approximated with an iterative method accounting losses thru convection, conduction and radiation (chapter 3.5.5). Thru this, it is possible to show which effects are the dominant and to approximate which average temperatures are reached in the different parts of the setup.

3.5.2 Pulse Energy and corresponding temperature rise

Since the average power of the laser is only regulated by varying the pulse width, the glass still experiences the full pulse power. With the thermal properties of fused silica given in chapter 2.1.2, the effect of one pulse in the disc can be simulated.

For laser radiation, MITRA [24] recommends a one-dimensional solution of the FOURIER equation. Due to the high absorption of fused silica at the used wavelength, it is valid to assume that all energy is absorbed at the surface. The Temperature for penetration depth (z) and time (t) can then be calculated as:

$$T(z,t) = \frac{\frac{P_L \cdot t}{A_{beam}}}{2 \cdot \rho \cdot c_p \sqrt{\frac{\pi \cdot \overline{\lambda}_{FS} \cdot t}{\rho \cdot c_p}}} \cdot \exp\left\{ -\frac{z^2 \cdot \rho \cdot c_p}{4 \cdot \overline{\lambda}_{FS} \cdot t} \right\}$$

Equation 13 *One-dimensional solution of the FOURIER equation to calculate the temperature pattern.*

where P_L is the pulse power, A_{beam} is the irradiated area, ρ is the density of fused silica, c_p its specific heat capacity and $\overline{\lambda}_{FS}$ the mean thermal conductivity at temperatures between 20°C and 300°C. Figure 18 shows the temperature pattern in time and depth for a time of 30µs and a depth of 10µm.

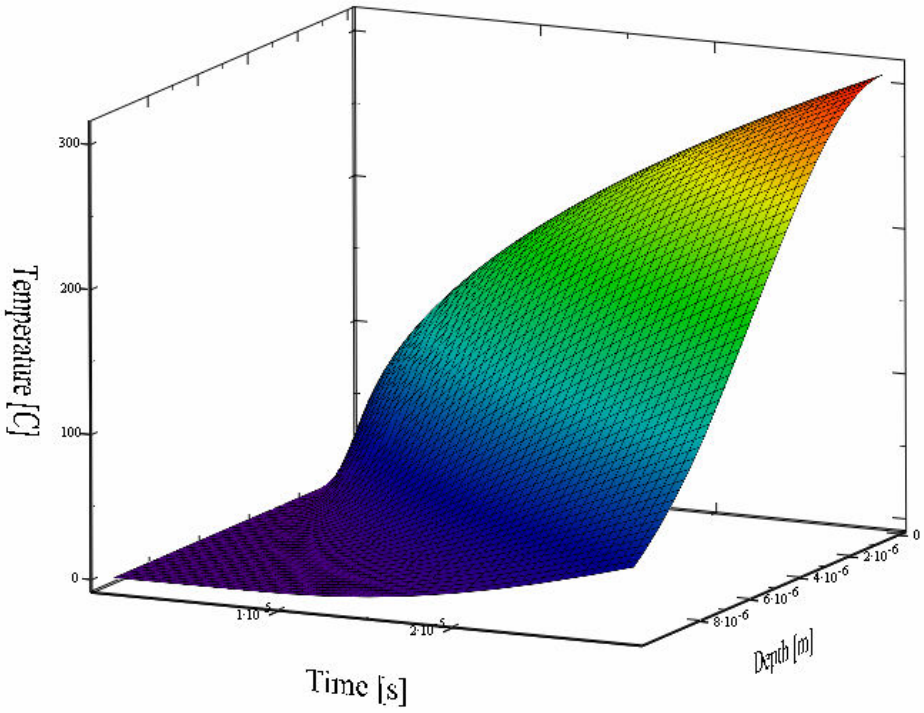

Figure 18 *Temperature pattern on the disc surface for a depth of up to 10µm and 30µs when irradiating with 64W.*

The calculation shows how the energy of the laser beam is accumulated on the surface. At the end of a 30µs pulse, the surface has reached nearly

300°C. The penetration inside the material is described by the exponential part of Equation 13. It can be seen in Figure 18.

During the welding process, circles are scanned at high speed. The material will heat up slowly. When a laser pulse hits the already warmed up glass, the heat has not enough time to spread and is accumulated at the surface. For a short time, high temperatures may be reached at the area of impact. If the intensity is too high, this leads to temperatures above the boiling point of fused silica and massive vaporization. This was observed with average laser power above about 8W. For the calculation below, a pulse width of 23µs is used, which resembles an average laser power of 7.2W. This setting proofed to be the maximum laser power to keep vaporization low.

3.5.3 Thermal relaxation time

An important factor for laser applications is the thermal relaxation time. It is a measurement for how fast the temperature decreases in a specific area due to heat transfer. As shown in chapter 2.2.2.3, this is of special interest for glass applications. When working with a pulsed laser, it must be tried to achieve heat accumulation in the working area. Thus, the pulse period must be adjusted to the thermal relaxation time.

The definition of thermal relaxation time is gained from the solution of the FOURIER equation (Equation 13) mentioned above. It is defined as the time, at which the exponential part in the solution becomes –1 for the absorption depth of the laser radiation. The latter can be calculated after CROOKS [7]:

$$\beta = \frac{1}{\alpha} = \frac{\lambda}{4 \cdot \pi \cdot k_{ex}}$$

Equation 14 *Calculation of absorption depth.*

with α as the absorption constant, λ as the wavelength and k_{ex} as the extinction coefficient (see chapter 2.1.2).

The absorption depth in fused silica for 10.6µm wavelength is 34µm.

Using this in the exponent of the solution above as depth z and dissolving to t, the thermal relaxation time can be calculated as:

$$\tau_R = \frac{\beta^2}{4 \cdot \kappa}$$

Equation 15 *Calculation of thermal relaxation time*

The thermal relaxation time for fused silica is 678µs. The pulse period should not be bigger than the thermal relaxation time to allow the energy of the pulsed laser to accumulate. For the experiments, a pulse period of 200µs is used. Concordantly, the material does not cool down significantly in between two pulses and the heat may accumulate.

3.5.4 Heat transfer

3.5.4.1 Radiation

Radiation strongly depends on the temperature difference between the medium and its surrounding. Assuming, that fused silica acts as a black body [21], heat loss thru radiation is described by:

$$\dot{Q}_\sigma(T) = \sigma \cdot A_\sigma \cdot \left(T^4 - T_S{}^4\right)$$

Equation 16 *Radiative heat flow*

with σ as the STEFAN'S constant ($\sigma = 5.67 \cdot 10^{-8} \frac{W}{m^2 K^4}$), A_σ as radiating area, T as the temperature of the glass and T_S as the temperature of the surrounding.

Increasing with temperature in the fourth potency, radiation usually dominates at high temperatures.

3.5.4.2 Convection

The losses thru convection are described by the following equation:

$$\dot{Q}_\alpha(T) = \alpha_C \cdot A_\alpha \cdot \left(T - T_S\right)$$

Equation 17 *Heat flow thru convection*

with A_α as the active surface and α_C as the convective heat transfer coefficient. It depends on the surface condition and the surrounding

atmosphere. For a polished surface with natural convection (no flow), α_C is given as $5.6\frac{W}{m^2K}$ [19].

The same Formula will be used in the calculations to simulate the temperature flow into the aluminum contact area. Although, this is a conductive heat transfer, the transit to the aluminum is described by the same equation like the transit to the air by convection. For the transfer to the aluminum, the heat transfer coefficient for still water on a metal surface is used: $\alpha_{Alu} = 350\frac{W}{m^2 \cdot K}$ [19]. This is the closest match to the conditions that was found.

3.5.4.3 Heat conduction

The geometry of the disc is described by using cylindrical coordinates. Here, the cross sectional area increases with increasing radius. With all other variables constant, heat conduction in the disc only depends on the radius and is therefore one-dimensional. The change of cross sectional area with radius can be described by using the logarithmic mean of the cross sectional areas in between which the conduction takes place [22].

$$A_\lambda = \frac{A_{C\max} - A_{C\min}}{\ln(A_{C\max} / A_{C\min})}$$

Equation 18 *Logarithmic mean of the minimum and maximum cross sectional areas.*

where $A_{C\min}$ and $A_{C\max}$ are the minimum and maximum cross sectional areas.

The heat flow thru the length l_λ is then described by:

$$\dot{Q}_\lambda(T) = \overline{\lambda}_{FS} \cdot \frac{A_\lambda}{l_\lambda} \cdot (T - T_S)$$

Equation 19 *Amount of heat lost thru conduction in radial geometry*

Where $\dot{Q}_\lambda(T)$ is the heat flow thru the logarithmic mean cross sectional area A_λ and $\lambda_{FS}(T)$ is the thermal conductivity. It depends on temperature as described in chapter 2.1.3.4. The used iterative method allows choosing the appropriate value for every increment.

3.5.4.4 Heat transfers in the disc

The different heat transfers shall now be compared for the radial geometry of the disc. Please note, that this is only a rough approximation to compare the three mechanisms of heat transfer.

Thermal conduction in a radial geometry is calculated by using the logarithmic mean of the inner and outer cross sectional areas thru which conduction takes place (Equation 18). The inner cross sectional area is calculated for a radius of 0.5mm. This is the radius up to which the surface was observed to be melted during the experiments with a circle diameter of 0.8mm. It shall therefore be referred to as the radius of the melt $r_{melt} = 0.5mm$ (see Figure 19 below). The outer cross sectional area is the outer edge of the disc. The length of conduction (l_λ) is the distance between inner and outer cross sectional area. Temperature dependence of the thermal conductivity is accounted by using Equation 2 for the present temperature. For the comparison, conduction is approximated assuming that the edge of the disc remains at room temperature. It depends on the temperature difference so a more accurate method is used for later calculations.

Figure 19 gives an overview of the used measurands for the calculations.

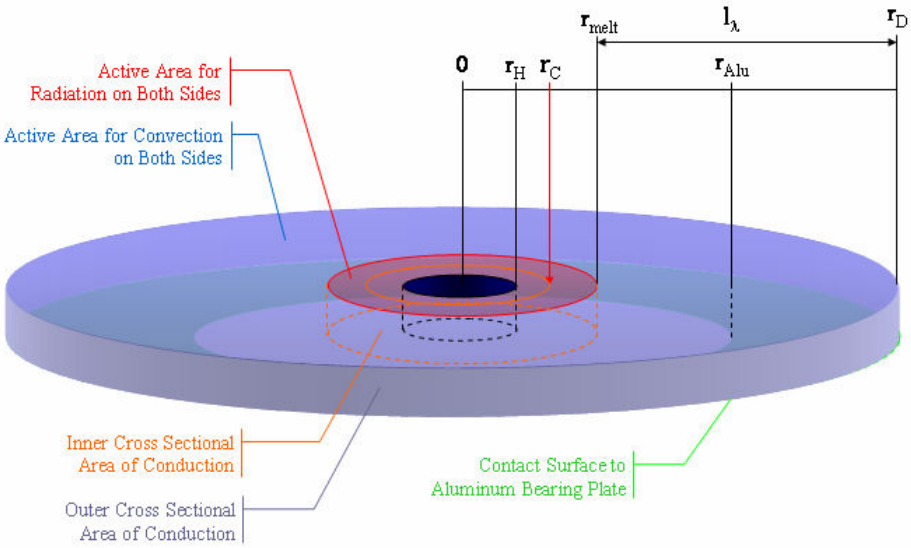

Figure 19 *Measurands for the calculations*

The radiating area was approximated as the melted surface. Depending on temperature in the fourth potency, the radiation should be calculated

for every radius separately. Without knowing the temperature at every radius, the radiative loss is approximated by calculating only the radiation of this melted surface using one temperature. This is the hottest area and since radiation strongly depends on temperature, it is the biggest part of the radiative losses.

Convective losses only play a small role. Since their dependence on temperature is low, it is legitimate to use the whole disc surface for their calculation.

The three different mechanisms of heat transfer have a different dependence on temperature. While convective heat transfer increases linear with temperature, the radiative heat transfer rises with the fourth potency of temperature and the conductive heat transfer varies with the thermal conductivity after Equation 2. Figure 20 shows a comparison of the occurring losses for the radial geometry of the disc.

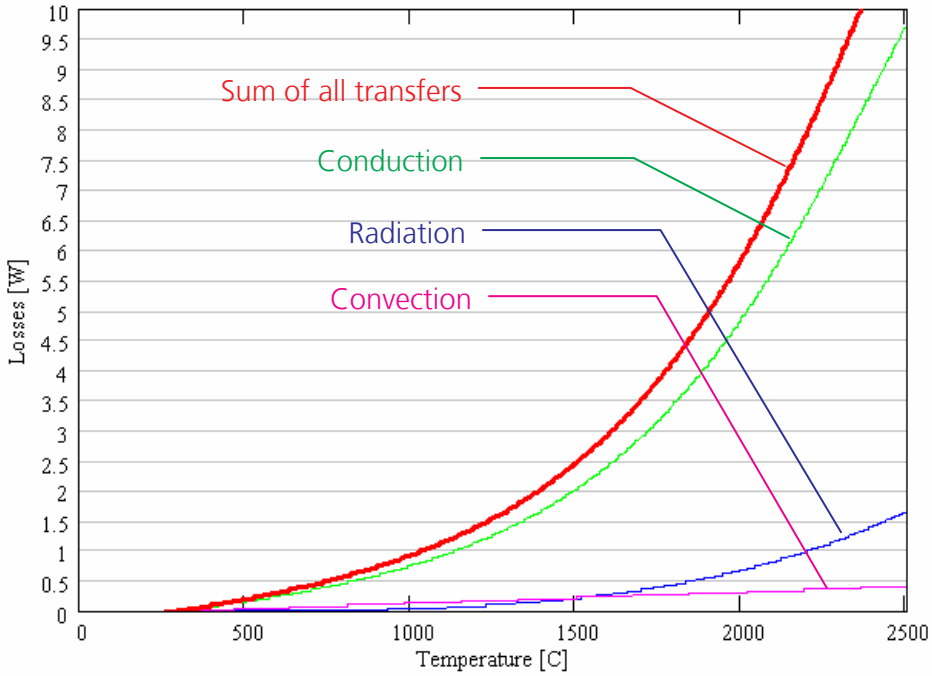

Figure 20 *Comparison of occuring losses exemplified at the heat flow in the disc.*
--: Convection
--: Conduction
--: Radiation
--: Sum of all transfers

The approximation already shows, that the loss thru conduction clearly dominates the process. Although it is referred to as loss, it is evident for the success of the experiments. Good thermal conduction is needed to heat up the inner part of the disc and melt it in the whole depth.

Radiation, which usually dominates at high temperatures, is comparably low because of the small radiating area.

3.5.5 Calculation of temperature during heating and cool down

As shown above, the losses all depend on the actual temperature. Therefore, an iterative method is used to simulate the temperature progression. It allows the losses to be calculated for the actual temperature of every calculation step. They must be regarded as negative powers since they dissipate energy from the material. Equilibrium is reached when the amount of heat lost equals the amount of heat inserted by the laser. Conduction clearly is the limiting factor for the temperature reached in the glass. Since it depends on the temperature

difference, the temperature at the outer edge of the disc is approximated with an iterative method first using a constant inner temperature and then used for the conductive loss to calculate temperature at the laser impact area.

The temperature is calculated by applying the resulting power (inserted power – losses) to a certain mass of fused silica with its corresponding heat capacity. This method implicates, that the power is inserted into the whole mass instantly. This is not the case here since the laser energy is absorbed on the surface and then propagates into the material. The calculation must therefore be understood as an approximation of the average temperature reached in the mass. The calculation of the temperature of the outer edge for example uses the whole mass of the disc outside the melted radius. The temperature at the outer edge will be lower than the calculated value.

3.5.5.1 Approximation of temperature of the outer edge

The following parameters are used to calculate the temperature of the outer edge of the disc:

- The temperature at the radius of the melt (r_{melt}) is approximated as constant 2000°C.
- The thermal conductivity to the edge is calculated with the mean thermal conductivity of the present temperature range after Equation 2 and Equation 3:

$$\overline{\lambda}_{FS.i} = \frac{\int_{T_{Edge.i}}^{T_{melt}} 0.78 - 0.054 \cdot e^{\frac{T+379}{354}} + 0.165 \cdot e^{\frac{T+379}{405}} dT}{T_{melt} - T_{Edge.i}}$$

- The length of conduction is $l_\lambda = r_D - r_{melt} = 1.8mm$, which is the distance between the melted center and the edge.
- The logarithmic mean cross sectional area of this length is (Equation 18):

$$A_\lambda = \frac{A_{\lambda Edge} - A_{\lambda melt}}{\ln\left(\frac{A_{\lambda Edge}}{A_{\lambda melt}}\right)}.$$

- The heat flow of conduction is then:
  $$Q_{\lambda.i} = \overline{\lambda}_{FS.i} \cdot \frac{A_\lambda}{l_\lambda}\left(T - T_{Edge.i}\right)$$

- Convection losses are calculated for the surface area of the disc from the melted zone to the edge. The temperature of the surrounding (T_S) is constant at room temperature:
  $$\dot{Q}_{\alpha.i} = \alpha_C \cdot A_C \cdot \left(T_{Edge.i} - T_S\right)$$

- Radiation losses are calculated for the same area $A_R = A_C$:
  $$\dot{Q}_{\sigma.i} = \sigma \cdot A_R \cdot \left[T_{Edge.i}{}^4 - T_S{}^4\right]$$

- Conductive losses to the aluminum bearing plate are calculated with the heat transfer coefficient of still water on metal.
  $$Q_{Alu.i} = \alpha_{H2O} \cdot A_{Alu} \cdot \left(T_{Edge.i} - T_S\right)$$

- The heat capacity of the glass is calculated for the mass of the disc outside the melted zone m_{Edge}.

- After two seconds, the cool down process is simulated by setting the heat conduction from the melted zone to 0W

Figure 21 shows these parameters and the losses schematically.

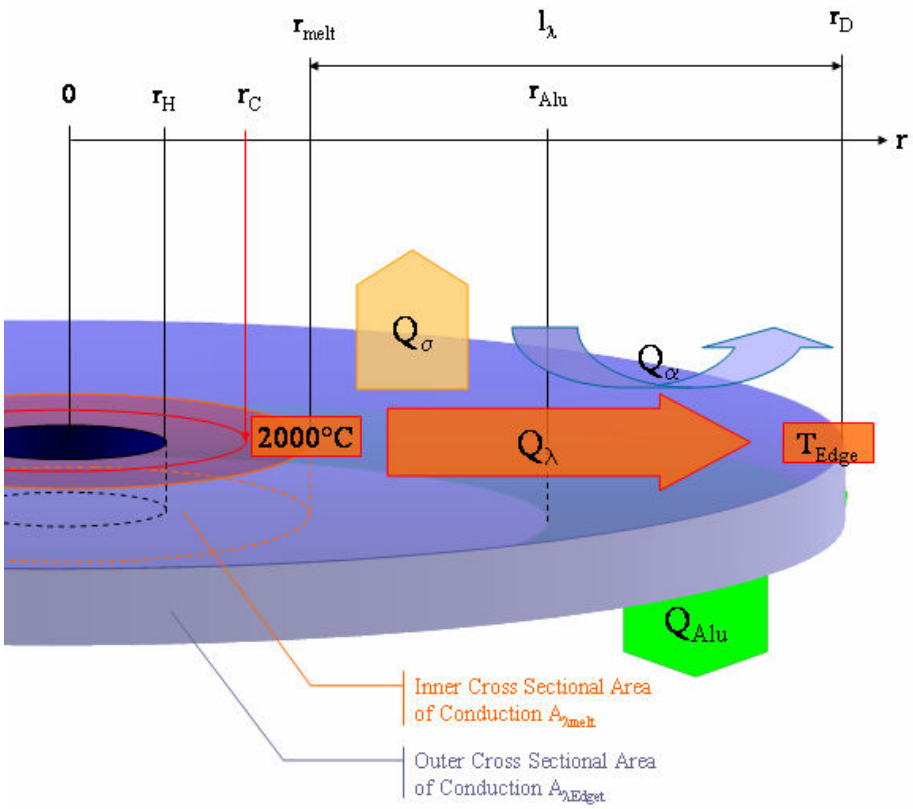

Figure 21 *Schematic illustration of the calculation of the edge temperature.*

The temperature of the discs edge may now be calculated as:

$$T_{Edgei+1} = T_{Edgei} + [\dot{Q}_{\lambda.i} - \dot{Q}_{\sigma.i} - \dot{Q}_{\alpha.i} - \dot{Q}_{Alu.i}] \cdot \frac{\Delta t}{c_p \cdot m_{Edge}}.$$

with Δt as time increment for the calculation.

Figure 22 shows the temperature progression delivered by the calculation. The edge reaches equilibrium at a temperature of about 950°C when the melted zone has a constant temperature of 2000°C. After two seconds, the cool down process is simulated by setting the heat conduction from the melted zone to 0W. The high conductive loss to the aluminum bearing plate leads to a rapid cooling down of the disc at the edge. It reaches room temperature after approximately 0.3 second.

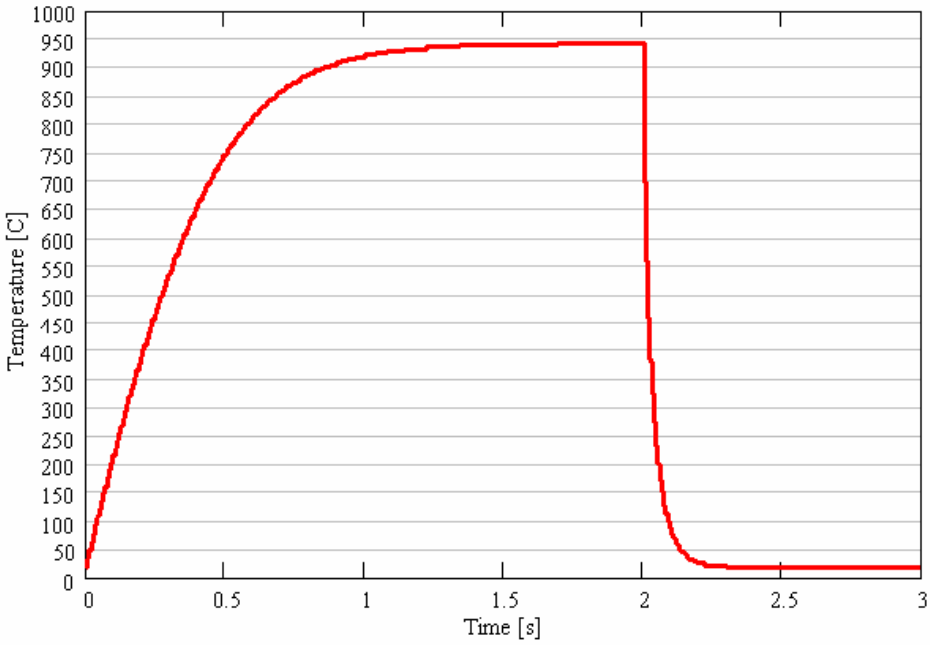

Figure 22 *Approximation of the temperature progression at the outer edge of the disc*

This temperature progression is now used to calculate the losses thru heat conduction from the melted center to the edge when calculating the temperature there.

3.5.5.2 Calculation of temperature in the melted zone

The temperature at the impact area is calculated using the same method like before. Running the same index, the calculation uses the present temperature of the edge calculated above for every iteration step. By this, the calculation of heat conduction becomes much more accurate than the approximation made in chapter 3.5.4.4.

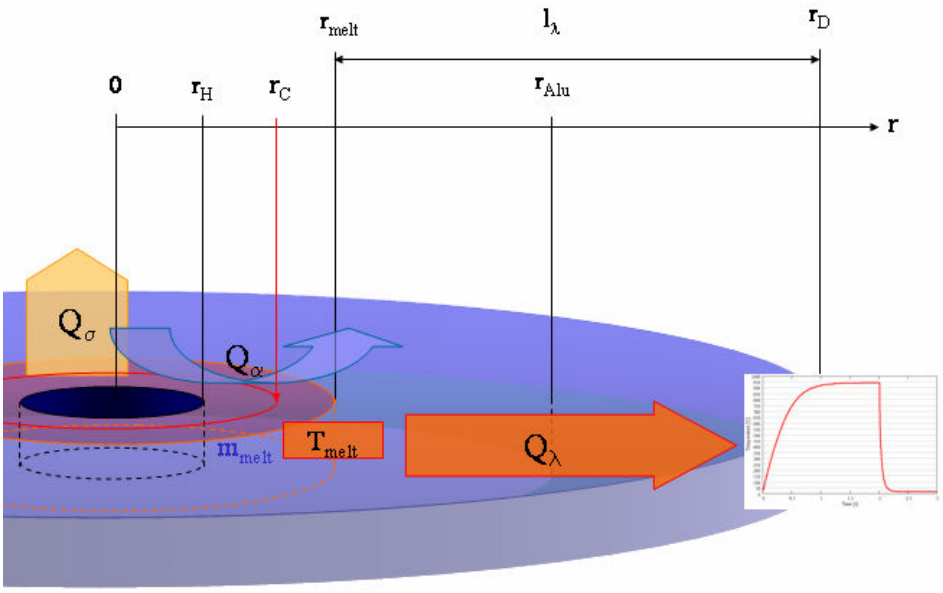

Figure 23 *Schematic illustration of the temperature calculation at the area of impact*

The following parameters are used:

- The average laser power is about 7.2W. This is a setting discovered experimentally. The laser power heats the whole mass used for calculation simultaneously.
- The calculation of the thermal conductivity to the edge is the same as before, only now it is considered a loss and therefore negative. It uses the temperature propagation of the edge described above and the same parameters.
- The melted area $A_{melt} = \pi \cdot (r_{melt}{}^2 - r_H{}^2)$ is used as active surface for convection as well as radiation $A_\alpha = A_\sigma = 2 \cdot A_{melt}$.
- Radiation losses are:
  $\dot{Q}_{\sigma.i} = \sigma \cdot A_{melt} \cdot \left[T_{melt.i}{}^4 - T_S{}^4\right]$
- Convection losses are:
  $\dot{Q}_{\alpha.i} = \alpha_C \cdot A_{melt} \cdot \left(T_{melt.i} - T_S\right)$
- The mass m_{melt} is approximated as the whole disc material of the melted Area: $m_{melt} = A_{melt} \cdot h_D \cdot \rho$.

- The laser power is set to 0W after 2 seconds to simulate a cool down process.

The temperature in the melted zone may then be calculated as:

$$T_{i+1} = T_i + \left[P_L - \underbrace{\sigma \cdot A_R \cdot \left[T_i^4 - T_S^4\right]}_{\dot{Q}_\sigma} - \underbrace{\alpha_C \cdot A_C \cdot \left(T_i - T_S\right)}_{\dot{Q}_\alpha} - \underbrace{\bar{\lambda}_{FSi} \cdot \frac{A_\lambda}{l_\lambda}\left(T_i - T_{Edge}\right)}_{\dot{Q}_\lambda} \right] \cdot \frac{\Delta t}{c_p \cdot m_{melt}}$$

Equation 20 *Iterative calculation of temperature*

with Δt as time increment for the calculation. Figure 24 shows the result of this calculation.

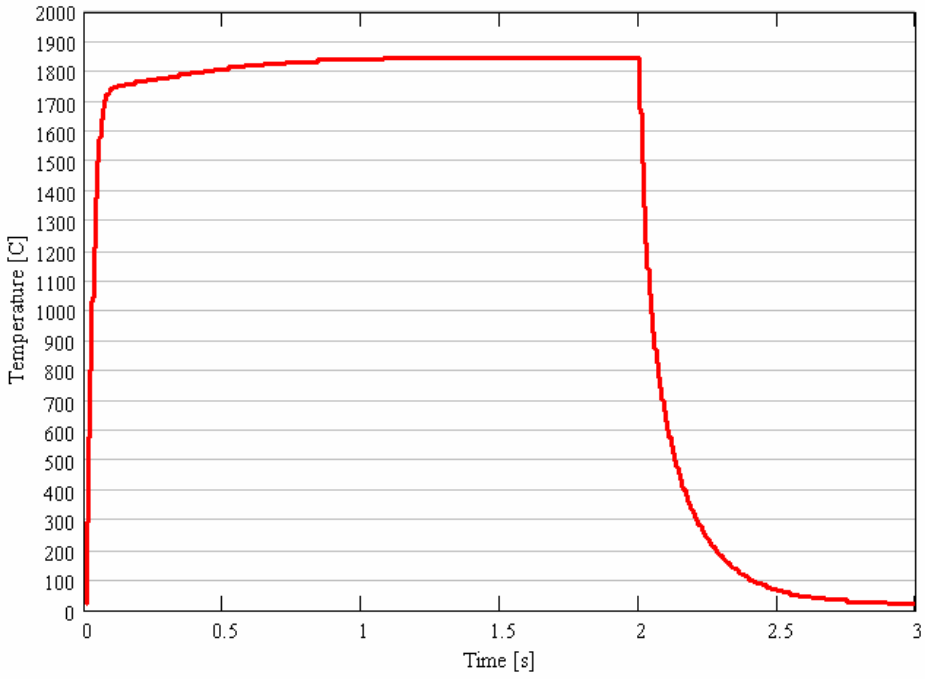

Figure 24 *Simulation of the temperature development in the glass. The steep rise is limited by the growing loss thru conduction. It keeps rising slowly until equilibrium is reached at nearly 1900°C. When setting P_L to 0W after 2s, the high conductive loss leads to a steep decline of temperature before its effect weakens at lower temperatures.*

The temperature rises steeply before the growing losses thru conduction slow it down. It slowly increases further until the edge of the disc has

reached its equilibrium, too. Now, the sum of all losses equals the energy inserted by the laser. A temperature of nearly 1900°C is reached after about one second. When welding, this temperature is held for about 14 seconds but to demonstrate the cooling down, the laser power is set to 0W after 2 seconds already in the calculation.

It must be perceived, that this is an approximation only. This calculation assumes that the energy of the laser spreads in the whole melted zone instantly increasing temperature in the whole depth. In fact, a temperature gradient forms as shown in chapter 3.5.2. The temperature at the discs surface must be higher than the temperature calculated here. Experiments showed that with an increase of laser power above the value used for calculation, vaporization of the material increases rapidly. It is therefore believed, that then temperatures above the boiling point of 2230°C are reached at the laser impact.

When cooling down, the high conductive loss leads to a steep decline of temperature before its effect weakens at lower temperatures. The glass cools down by about 1800°C in only 0.5 seconds, leading to a cooling rate of about 3600K/s. Although, this is only a rough approximation of the cool down process, it is obvious that the minimum cooling rate of $9 \cdot 10^{-6}$ K/s, needed to avoid devitrification, is surpassed by far. No additional cooling is needed.

3.5.5.3 Calculation of temperature at inner edge

To establish a connection between disc and fiber, the edge of the hole must be melted. To simulate the temperature progression at the hole, the same method as above is used again. The heat now flows from the radius of laser impact (0.4mm) to the radius of the hole (0.2mm) with the corresponding length, cross sectional area and mass. The temperature at the radius of laser impact shall be the temperature of the melted zone calculated above. The mass of the disc from the radius of impact to the hole is used for the calculations. This is valid to make an approximation for the temperature because the temperature crosses this volume to reach the inner edge.

Figure 25 shows a schematic illustration of the heat flow in the inner part of the disc.

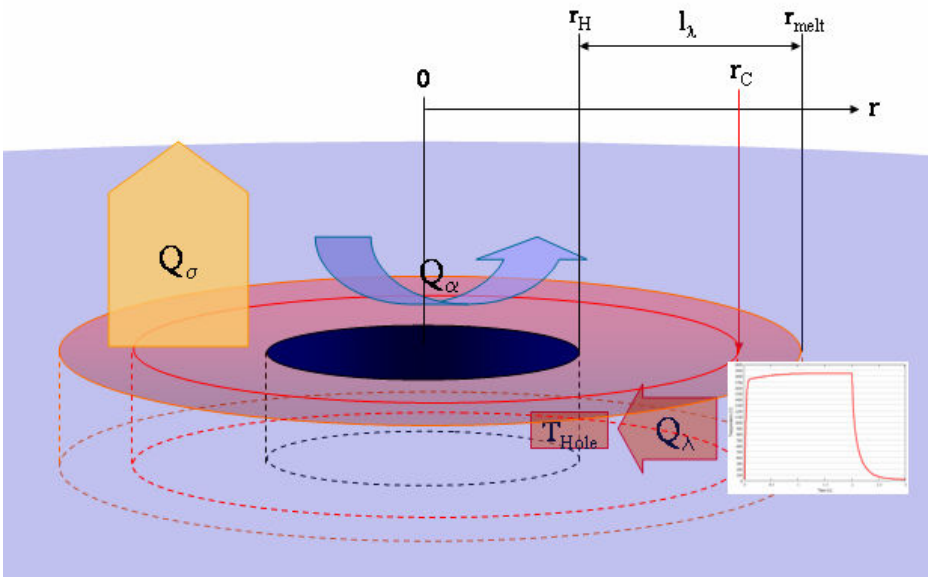

Figure 25 *Schematic illustration of the temperature calculation at the inner edge*

Figure 26 shows the temperature pattern at the hole. It must again be noted, that the simulation cannot resemble the actual temperature. Temperature accumulation at the edge is not simulated. In reality, especially the temperature at the top of the disc will be higher than calculated. Nevertheless, the calculation shows very nice that temperature at the inner edge increases nearly as fast as at the area of impact, having only a slight delay. Equilibrium is reached at 1400°C after one second already. This temperature is remarkably lower than the one calculated for the area of impact. Conduction to the outer edge of the disc and losses thru radiation and convection prevent a higher temperature at the inner edge. This complies with the discoveries made during the experiments. Since laser radiation is absorbed on the surface, the temperature spreads in the top of the disc faster but due to high losses, the heat does not reach the bottom of the 300µm disc leading to an insufficient penetration depth (see chapter 4.1.3).

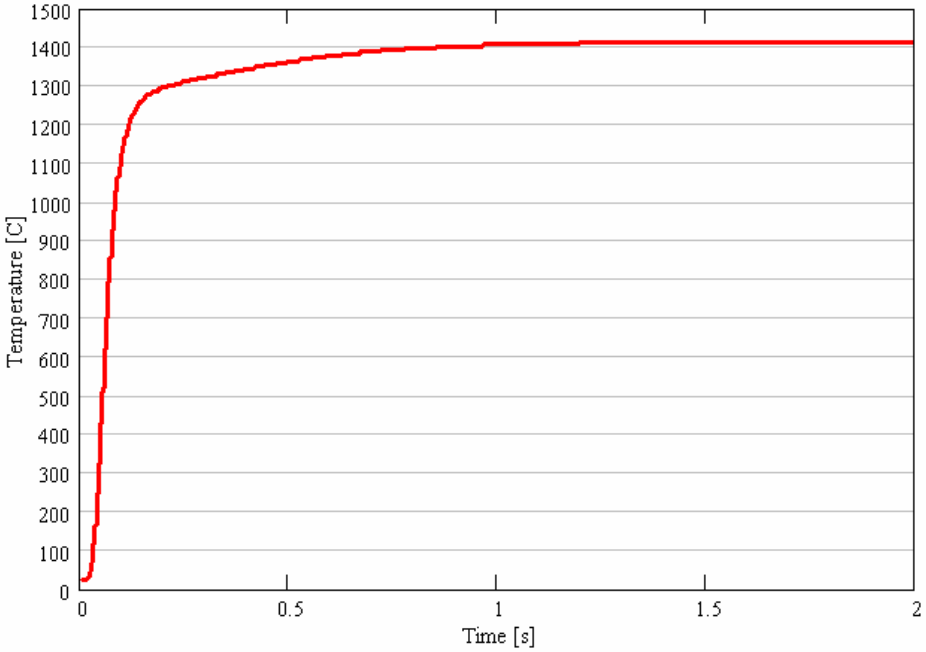

Figure 26 *Simulation of the Temperature rise at the hole. The temperature reaches equilibrium at 1400°C already after about one second.*

3.5.5.4 Heat transfer to the fiber

When no connection between fiber and disc is established, the gap between disc and fiber can only be transcended thru convection and radiation. This process is now simulated using the temperature calculated above. Radiation is calculated as mentioned above. The corresponding areas are the inside of the hole and the opposing fiber surface. Since the gap is very narrow, the discs radiation will hit the fiber entirely.

Heat transfer thru the gap is described by two equal coefficients of convection (Disc-Air and Air-Fiber) $\alpha_C = 5.6 \frac{W}{m^2 \cdot K}$ and the heat conduction in air $\lambda_{air} = 0.02 \frac{W}{m \cdot K}$ [19]. Those three coefficients can be written in one as [17]:

$$k_{gap} = \frac{1}{\frac{2}{\alpha_C} + \frac{w_{gap}}{\lambda_{air}}}$$

Equation 21 *Combined constant for heat transfer thru the gap by convection.*

The width of the gap is $w_{gap} = 13.5\mu m$, assuming that the fiber is perfectly centered with an even gap all around. The heat flow thru the gap by convection is calculated as:

$$\dot{Q}_{Cgap} = k_{gap} \cdot A_{gap} \cdot \left(T_{Disc} - T_{fiber}\right)$$

Equation 22 *Heat flow thru the gap*

with A_{gap} as the inner surface of the hole: $A_{gap} = \pi \cdot d_H \cdot h_D$ and the temperatures of disc (T_{Disc}) and fiber (T_{fiber}).

Radiation is calculated as before. Again the radiating areas are the same as for convection.

The only loss accounted in the fiber is the heat conduction in z-direction. Its cross sectional area is the cross sectional area of the fiber: $A_{\lambda fiber} = \pi \cdot r_F{}^2$. The heat is conducted in both directions. As length of conduction, 2mm is used. This was used as the length of fiber over the disc before. The loss thru heat conduction occurs in both directions of z. Therefore, it occurs in Equation 23 twice. The temperature at the end of the fiber shall be constant 20°C.

Using the temperature of the hole calculated above, the temperature of the fiber is calculated as:

$$T_{Fiber.k+1} = T_{Fiber.k} + \left[\dot{Q}_{Cgap.k} + \dot{Q}_{\sigma gap.k} - 2 \cdot Q_{\lambda Fiber.k}\right] \frac{\Delta t}{c_p \cdot m_{Fiber}}$$

Equation 23 *Temperature of the fiber*

The calculation delivers the temperature propagation given in Figure 27. The bad temperature transfer thru the gap prevents higher temperature. Equilibrium is reached at about 120°C. It is no doubt that this temperature cannot lead to a connection between fiber and disc.

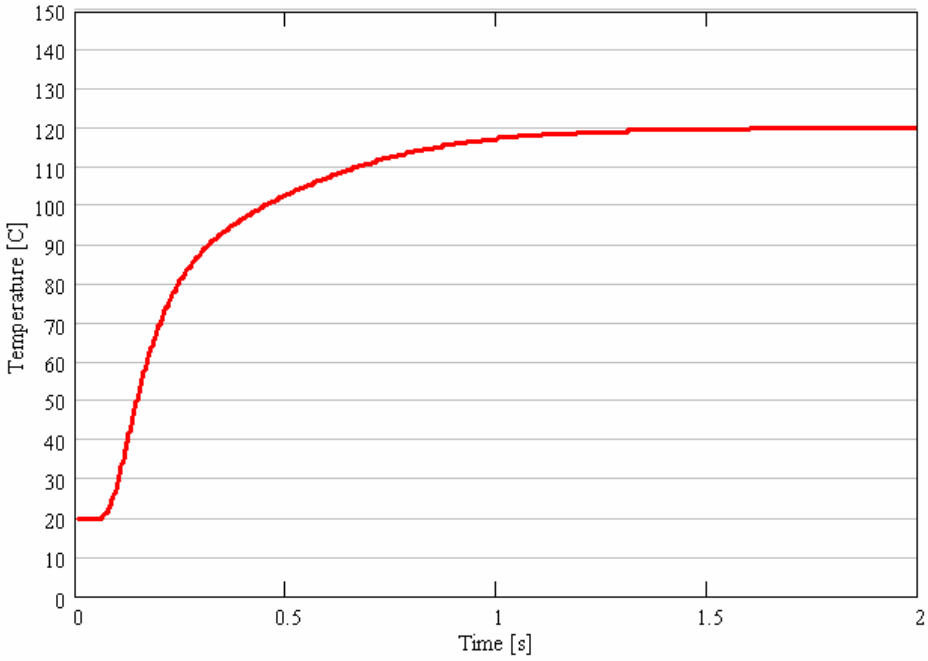

Figure 27 *Temperature propagation in the fiber. The bad heat transfer thru the gap limits the maximum temperature reached.*

This calculation, like the others, too, is only an approximation. It calculates the temperature of the whole fiber. For welding, it would be sufficient to melt the surface. Still, the temperature pattern shows that heat conduction thru convection and radiation are clearly not enough to melt the fiber. Only when a connection between fiber and disc is established, the much higher conductive heat transfer melts the fiber. This supports the discovery made during the welding experiments. Here, it was often not possible to establish a connection between fiber and disc. The problems occurring during the experiments are described in depth in the next chapter.

4 Welding experiments

4.1 Occurring problems

4.1.1 Fiber positioning

To guarantee a continuous connection, it is necessary to spread the energy of the beam evenly around the fiber, heating up the disc on its whole circumference equally. Otherwise, one side of the disc is melted first and surface tension may lead to the building of a hole. Since the fiber is clamped with coating, the fiber position is badly reproducible. The position of the scanned circle must be adjusted for every experiment. Since no aiming optic is available, this is only of limited success. The only possibility to adjust the circle position is to start the process and cancel it if a bad positioning is detected. The circle can never be positioned perfectly centrically and would sometimes even hit the fiber.

Altering the fixture to clamp the disc would avoid this. A fixed disc position is easier to achieve than a fixed fiber position.

4.1.2 Pyralyzation and Vaporization

As mentioned in chapter 2.1.3.1, fused silica begins to pyralyze at temperatures as low as 1350°C. Furthermore, heat accumulation on the glass surface can lead to temperatures above the boiling point of 2230°C. This effect was also described theoretically in chapter 3.5.2. Both effects may occur at the same time and can not easily be divided. Temperature measurement on the glass was not possible during these experiments so the effects of pyralyzation and vaporization had to be minimized experimentally. The forming of an undercut was experimentally researched by drawing blind seams on fused silica slides.

An undercut forms when either the intensity is too high or process times are raised to above about one minute. While the first effect should be due to heat accumulation on the glass surface and thru this vaporization, the second might be a result of increasing pyralyzation. The described band of haze, originating from the oxidized SiO or condensed vapor was observed after most experiments.

Vaporization can be minimized by limiting intensity on the glass, avoiding heat accumulation on the surface.

To minimize pyralyzation, process times should be minimized. To keep process times as low as possible, the energy must be kept high while intensity on the glass should not exceed a certain level to avoid vaporization.

To limit intensity and thru this vaporization, the beam is defocused by +4mm leading to an intensity on the surface of $I_S = 2515 W/mm^2$. A scanning speed of 455mm/s at a pulse period of 200µs leads to a beam overlap of 44% d_S. Vaporization was then observed to occur with average powers above about 8W.

With 7.2W and the speed and focus position mentioned above, more than 4000 scans were needed to establish a partly connection with the 300µm disc. With such long process times, pyralyzation still leads to an undercut at the beam impact. Further increase of process time merely improves results since the losses prevent a further spreading of temperature but worsens the effect of pyralyzation.

A typical example for such an effect can be seen in Figure 29 on page 65. Still using the 300µm disc, the number of scans was increased to 6000 here, leading to a deep undercut.

Using the 150µm disc, vaporization and pyrolyzation could be reduced to a minimum by decreasing average power and lowering process times.

4.1.3 Limited penetration depth

When welding metals with the laser, a plasma capillary usually builds up, enabling the radiation to be absorbed at the whole depth of the material. It may then spread evenly to the sides establishing a continuous connection. For glasses and especially for this setup, this is not possible. The radiation is absorbed at the surface and temperature must be given time to flow to the seam and melt the glass. Bearing in mind, that the whole disc from the impact of the beam to the edge and even parts of the fiber must be heated to above 2000°C by thermal conduction and at the same time, temperature on the surface must not exceed 2230°C to avoid vaporization, one can imagine that the whole process is quite sensible. The heat conduction process is shown schematically in Figure 28.

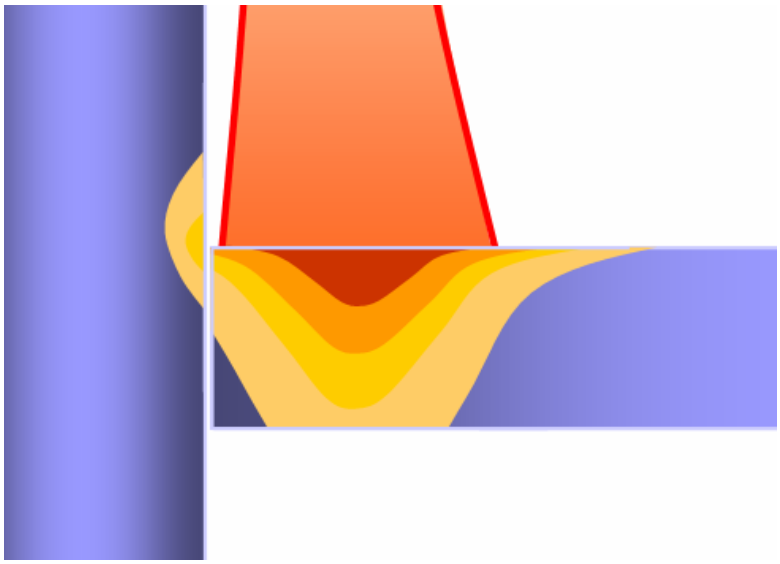

Figure 28 *Heat conduction in the disc. Hard to achieve sufficient penetration depth.*

The scanned circle radius can not be increased as mentioned above. Thermal conduction is therefore the key to success for this experiment. Conversely, as shown in the calculations, the high losses lead to rather low temperatures. Especially the lower part of the disc needs a long time to heat up or might never reach a sufficient temperature. With the 300µm disc, for example, it was not possible to achieve sufficient penetration depth. This leads to a kerf between disc and fiber. A notch effect at this kerf made the connection very sensible to applied forces. Even the slightest touch would then lead to the breaking of the fiber at the kerf. Figure 29 shows a cross section of such an experiment. The fiber broke off at the kerf and pyrolyzation and vaporization led to the forming of a deep undercut.

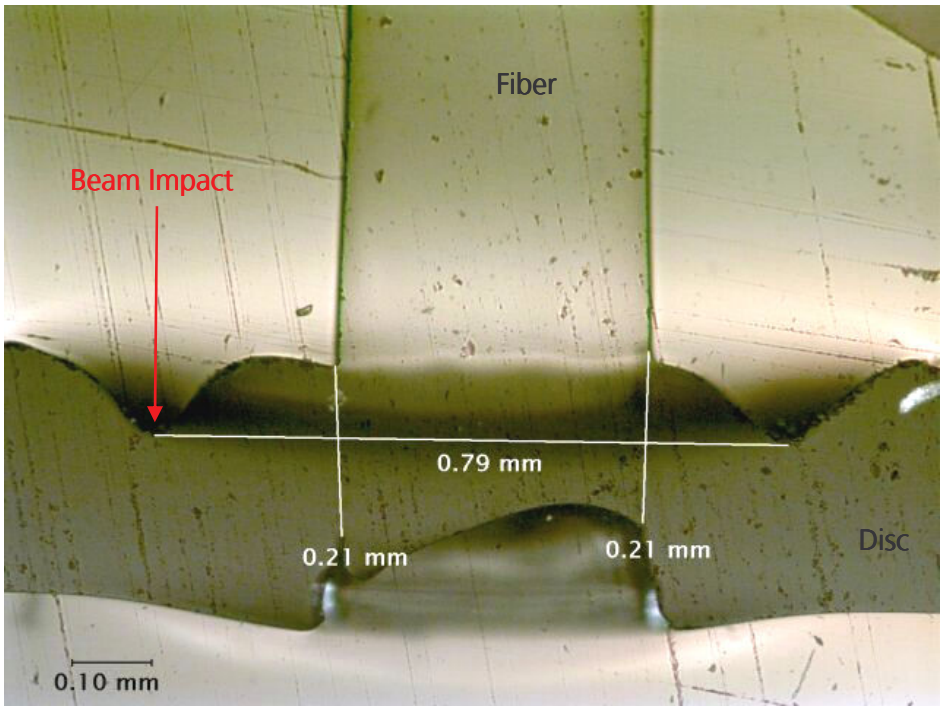

Figure 29 *Cross section of an experiment with a 300µm disc. Increased pyrolyzation and vaporization led to the forming of a deep undercut but still no sufficient penetration depth is reached. The fiber breaks due to a notch effect in the resulting kerf. [Microscope: Nikon Eclipse ME600, 100-times magnified; Photo: Spot Insight Color 3.2.0, Spot Advanced Software 3.2.4]*

The calculations showed, that heat conduction in the disc is problematic. Massive heat conduction to the outer edge of the disc leads to a low temperature reached in the inner part of the disc. With twice the thickness, the 300µm disc has twice the mass and heat capacity of the 150µm disc used for the calculations. The higher loss thru thermal conduction in the thick disc leads to even lower maximum temperature. The high process times could not improve the result since equilibrium was already reached. Figure 30 shows a comparison of the temperature reached with 150µm and 300µm thickness.

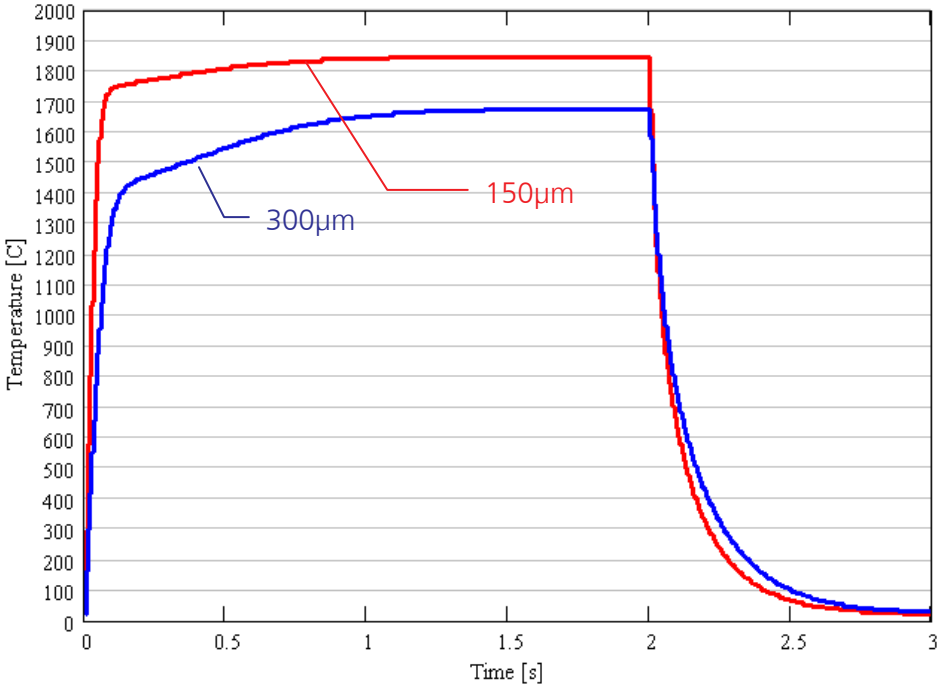

Figure 30 *Comparison of the temperature reached in the disc with 150µm and 300µm thickness [-- 150µm, -- 300µm]*

With the given setup, a solution to the problem is increasing the beam diameter on the surface, allowing a higher laser power while keeping intensity on the disc constant. To avoid damage to the fiber, it is then necessary to increase the distance from the seam. This is contra productive because the heat has to cross a bigger distance and even more material has to be melted. Experiments approved this.

The changed experimental setup described in chapter 4.2 might be a solution for this problem because it allows bigger beam diameters allowing to join the 300µm disc on the whole depth as well. A first solution to this problem, however, is reducing the discs thickness. The fewer material of a thinner disc reduces heat capacity. With a connection in the whole depth, a radius of curvature on the joint improves the distribution of forces, leading to a higher stability.

The thinner discs have a thickness of 150µm. They allow the laser power to be reduced and a lower number of scans of only 1000

4.1.4 Withdrawing of disc due to surface tension

As mentioned in chapter 2.4, surface tension causes a liquid to minimize its surface area. Since a gap between disc and fiber cannot be avoided, this means that as soon as the glass is melted thru and no direct connection to the fiber exists, a spherical shape forms at the edge causing the glass to withdraw from the fiber. Figure 31 shows a cross section of a disc where the glass has withdrawn from the fiber. Furthermore, the groove where the directly hitting laser beam has vaporized some material is visual. It is not as deep as in Figure 29 anymore, since the number of scans could be reduced to 1000 and laser power was reduced to about 5.6W.

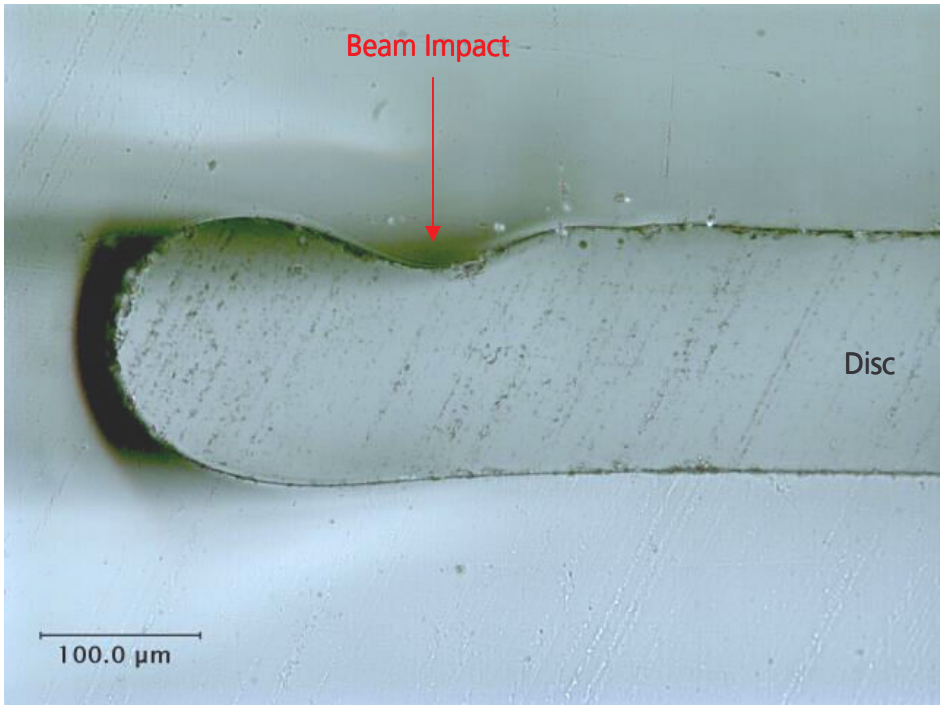

Figure 31 *Forming of a drop-like shape by the melted glass due to surface tension. The glass has withdrawn from the fiber without making a connection. [Microscope: Nikon Eclipse ME600, 200-times magnified; Photo: Spot Insight Color 3.2.0, Spot Advanced Software 3*

When the disc has close contact to the fiber, the same effect leads to the melt being drawn towards the fiber now minimizing the common surface area. A connection is then established at this point. Because of the radial symmetry, however, it is not possible to establish a contact all around. Where the connection is established first, the surface tension causes the liquid glass around the fiber to flow to this position. The material is then

missing on the other side of the fiber and a hole forms there. Figure 32 shows this process schematically.

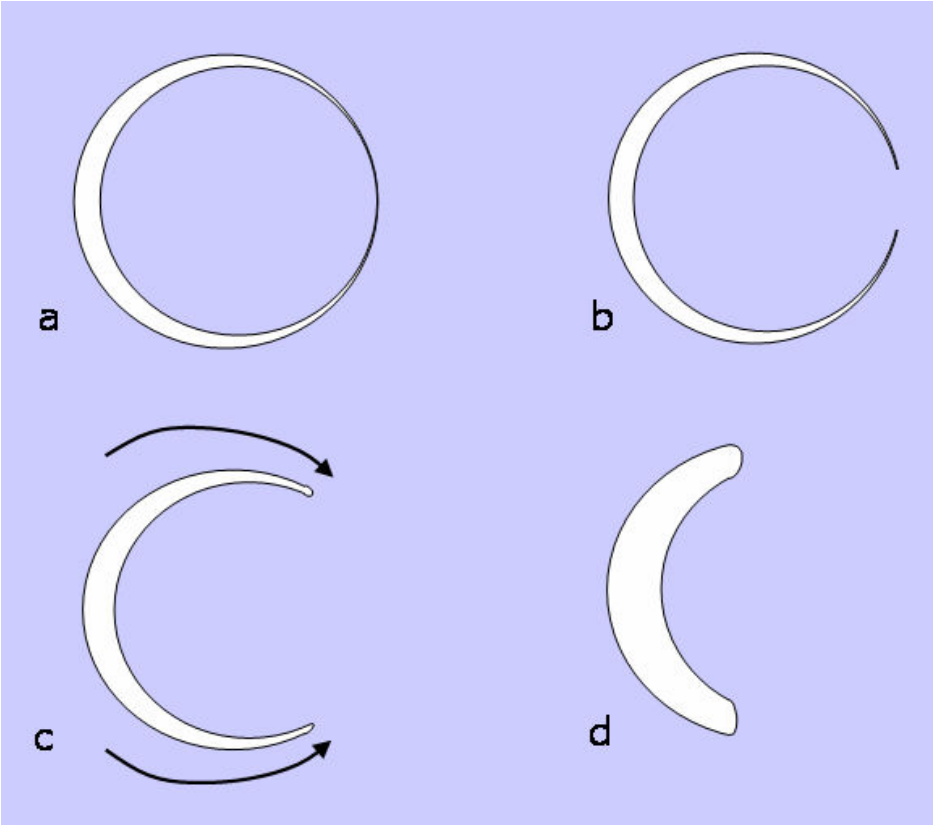

Figure 32 *Forming of a hole due to surface tension. a) Fiber has close contact on one side only. b) Disc melts on the whole circumference but can only connect where direct contact to the disc occurs. c) The melted glass of the opposite side flows towards the connection. d) A hole remains.*

Figure 33 shows a microscope picture of such a hole. Additionally, bubbles are visible opposite to the hole where the air of the gap did not have enough time to ascend and was "frozen in".

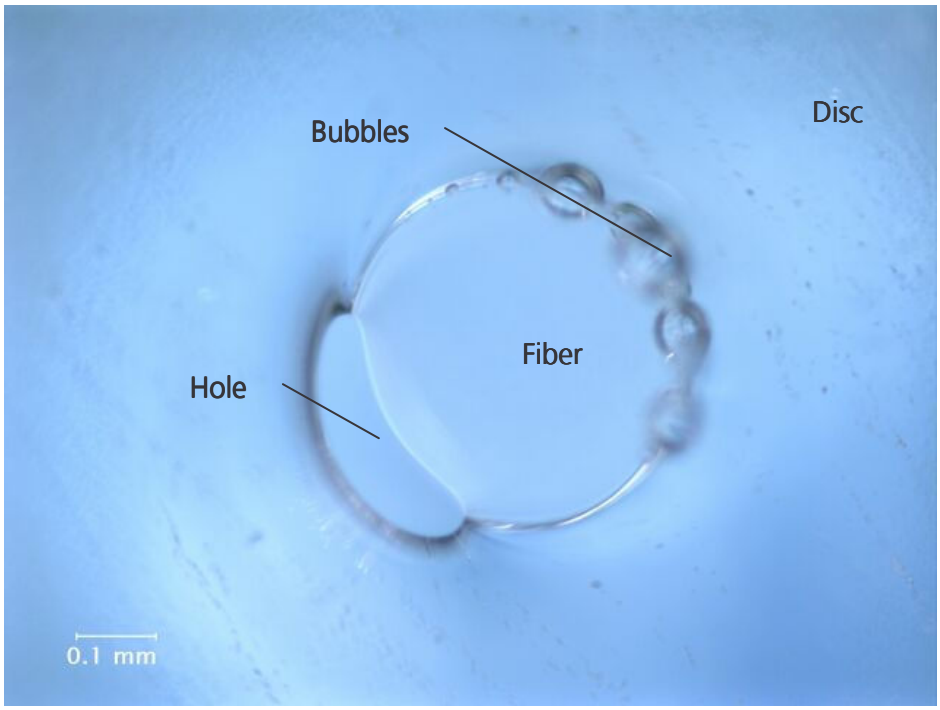

Figure 33 *Microscope picture of a hole that formed due to surface tension. Additionally, bubbles are frozen in the melt because they had insufficient time to ascend. [Microscope: Nikon Eclipse ME600, 100-times magnified; Photo: Spot Insight Color 3.2.0, Spot Advanced Software 3.2.4]*

Increasing the temperature of the melt would lower viscosity and surface tension as described in chapters 2.3 and 2.4. However, considering that the viscosity of fused silica at elevated temperatures is still high, a further increase of temperature would rather lead to massive vaporization at the impact area than a better connection. While the freezing-in of bubbles can be avoided by increasing process time, the forming of the hole can only be prevented by using filler material. It was therefore decided to change the whole concept of the fiber connector as shown in the next chapter.

4.2 Changed experiment setup

As mentioned earlier, the thickness of the disc was reduced to 150µm. The number of scans and thru this the process time can then be reduced while keeping intensity high. The thinner disc is easier to melt in the whole depth. This however leads to a radius of curvature on the joint increasing stability.

The gap between fiber and disc was identified to be the biggest problem for the success of the experiment. It prevents heat transfer to the fiber. This makes it hard to establish a connection between fiber and disc on the whole circumference. If fiber and disc have contact, the much higher conductive heat transfer melts the fiber at this point. Once a connection is established, surface tension leads to the building of a hole.

The use of a scanner optic forces a distance between beam impact and groove as mentioned above. During the experiments it was not possible to change the setup in the way that the beam hits directly the groove. This, however, is one of the main reasons for numerous problems determined during the experiments. It must be tried to aim the beam directly on the groove. With the used setup, this is not possible without damaging the fiber.

Other than the original setup, it was therefore decided to aim the laser directly on the gap. Instead of avoiding damage to the fiber end, which was originally meant to already be polished, it is now completely melted. Not only allows this to heat up the seam directly, but also is the melted fiber now used as filler material. It fills the gap between fiber and disc and thru this allows a connection on the whole circumference. The changed setup is shown in Figure 34.

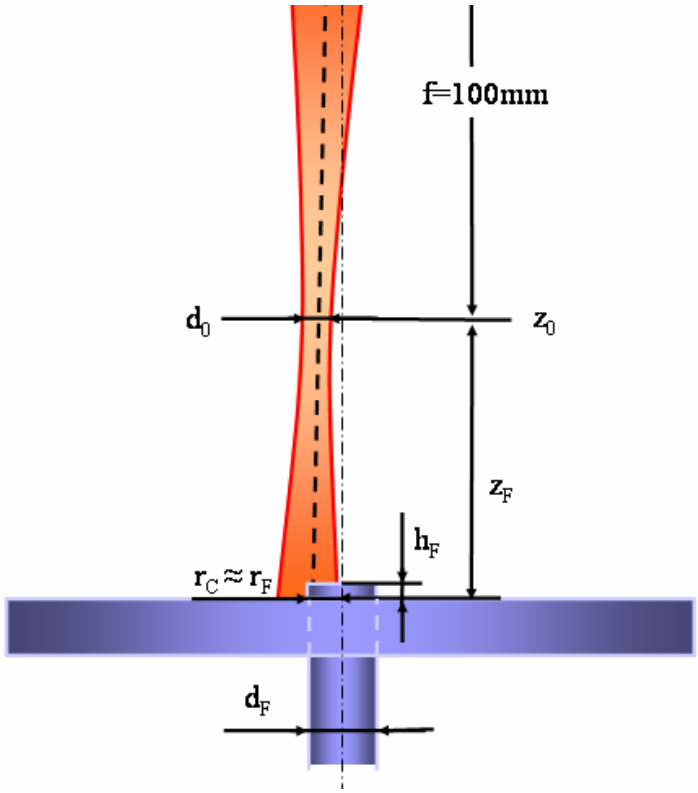

Figure 34 *Illustration of the changed experimental setup*

By further defocusing to $z_F = +6mm$ and reducing the scanned circle diameter to $d_c = 0.4mm$, the fiber end is melted. The changed settings lead to a direct heating of the fiber. Heat transfer thru the gap is not necessary anymore. The melted fiber flows into the gap. With the additional fiber material, holes are less likely to occur and a connection on the whole circumference is possible. The higher focus position also leads to a bigger spot area and thus lower intensity on the surface of 1118W/mm^2 compared to 2515W/mm^2 with the lower focus position. In combination with the reduced process time, this leads to a very low pyralyzation and vaporization. In fact, forming of an undercut is not observed anymore as seen in Figure 35 on page 73.

Different lengths of fiber were tested. It showed, that only very little fiber material is needed to fill the gap. The length of fiber above the disc can be adjusted under the microscope to about $h_F = 0.1mm$. After welding, only a small bulge remains. Fiber and disc can then both be polished and act as the fibers end surface.

Table 5 lists the parameters for the changed setup.

Parameter	Setting
Pulse Period	$PP = 200\mu s$
Pulse Width	$PW = 21\mu s$
Duty Cicle	$DC = \frac{PW}{PP} = 10.5\%$
Average Laser Power	$P_{AV} = 5.6W \pm 0.4W$
Pulse Energy	$E_P = P_L \cdot PW = 1.34mJ$
Focus position	$z_F = +6mm$
Beam diameter on surface	$d_S = 698\mu m$
Intensity on Surface	$I_S = 1118\frac{W}{mm^2}$
Scanning Speed	$v_s = 455\,mm/s$
Pulse Overlap	63%
Length of Fiber	$h_F = 0.1mm$
Scanned Circle Diameter	$d_C = 0.4mm$
Number of Scans	500
Total Process time	$t_p = 6.7s$

Table 5 *Parameter settings for the changed setup.*

5 Results

With the thin discs, a nice radius of curvature at the connection is achieved improving distribution of forces in the material and after changing the process setup, it was finally possible to achieve a good connection between fiber and disc. Figure 35 shows a cross section of a first example of such a connection.

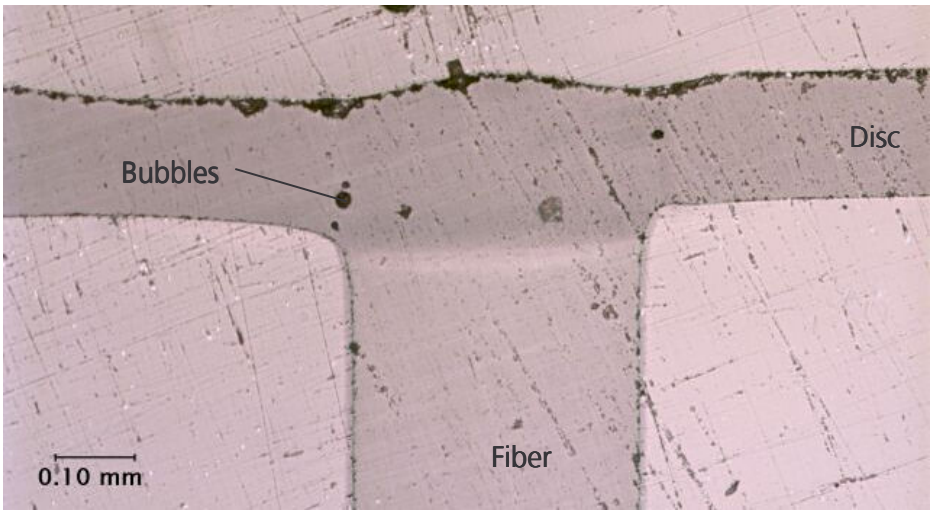

Figure 35 *Connection with melted fiber end. Small bubbles in seam should not impair beam quality. [Microscope: Nikon Eclipse ME600, 100-times magnified; Photo: Spot Insight Color 3.2.0, Spot Advanced Software 3.2.4]*

The few bubbles in the seam of Figure 35 should not degrade stability seriously and might be avoided by slightly increasing process time. The functionality as end cap remains unaffected since the light will not propagate to the very edge of the fiber. During these experiments, the end surface could not be polished. It can therefore not be guaranteed, that the process does not impair mode quality. Further testing is necessary here.

Still problematic is the reproducibility of the fiber positioning. It should be tried to either improve the clamping or install an aiming optic. It would then be possible to aim the drawn circle on the gap directly, melting disc as well as fiber.

6 Résumé

The unique properties of fused silica make it a hard to handle material. In combination with the complicated radial geometry of the seam, this made the experiment a challenging task.

While a few problems remain, the experiments can be rated as a success. It was shown, that a connection between fiber and disc can be established and most of the occurring problems were solved. The changed setup is a great step towards developing a stable process for manufacturing the fiber connector. Little more work should lead to a reproducible process delivering a strong connection and good optical properties.

For later manufacturing, it might be interesting to try other geometries or material combinations. Combinations of fused silica for example with Pyrex® glas was tried during other experiments with promising results. A different geometry would solve the problems connected with the radial geometry.

Bibliography

[1] BANSAL, NAROTTAM B.; "Handbook of glass properties"; Orlando: Academic Press, 1986; ISBN: 0120781409

[2] BEHLER, PROF. DR. ING. KLAUS; "Fokussierung von Strahlen"; Skript to "Laseranwendung Materialbearbeitung"; FH Giessen-Friedberg, Wilhelm-Leuschner-Straße 13, 61169 Friedberg/Hessen; 2001

[3] BEHLER, PROF. DR. ING. KLAUS; "Gaussscher Strahl"; Skript to "Laserphysik"; FH Giessen-Friedberg, Wilhelm-Leuschner-Straße 13, 61169 Friedberg/Hessen; 2002

[4] BRANDENBURG, K.; DIAMOND 2.1d, Crystal and Molecular Structure Visualization; Crystal Impact GbR, Bonn 2000

[5] CHEN, REUVEN AND PAGONIS, VASILIS; "Modelling thermal activation characteristics of the sensitization of thermoluminescence in quartz"; J. Phys. D: Appl. Phys. vol.36, 2003, pp. 1–6

[6] CHONG, JOO HIN and RAO, M.K.; "Development of a system for laser splicing photonic crystal fiber"; Optics Express, vol.11, no.12; June 2003

[7] CROOKS, D.; „Development of a CO_2 laser machine for pulling and welding of silica fibres and ribbons"; lecture held at the GEO 600 collaboration; Aspen, January 2005

[8] DIN ISO 7884 1-8; Glass - Viscosity and viscosimetric fixed points

[9] FRAUNHOFER USA, CENTER FOR LASER TECHNOLOGY; "Factsheet Glass Welding"; Center for Laser Technology, 46025 Port Street, Plymouth, MI 48170, Tel: (734) 354 6300, Fax: (734) 354 3335, laser@clt.fraunhofer.com, www.clt.fraunhofer.com

[10] FRIEDMAN, HERSHEL; "Crystal structure of SiO_2, Polymorphs of Quartz"; The Mineral And Gemstone Kingdom; http://www.minerals.net

[11] GALVANAUSKAS, A.; LIU, C.H.; EHLERS, B.; "*810-W single transverse mode Yb-doped fiber laser*", Advanced Solid-State Photonics meeting, Santa Fe, NM, USA, 2004

[12] GENERAL ELECTRIC COMPANY; GE Quartz, Inc., 4901 Campbell Road, Willoughby, OH 44094 USA, Phone: +1 (800) 438-2100, Fax: +1 (800) 258-3803; Homepage: http://www.gequartz.com/en/properties.htm

[13] GIBBS, PHILIP; "Is glass liquid or solid?"; Usenet Physics FAQ; http://math.ucr.edu/home/baez/physics/General/Glass/glass.html; January 1997

[14] GROVE F.J. and JELLYMAN P.E., "The infra-red transmission of glass in the range room temperature to 1400°C", *Journal of the Society of Glass Technology*, 39; transactions, 1955; pp. 3-15

[15] HARPER, CHARLES A.; "Handbook of ceramics, glasses, and diamonds"; New York : McGraw-Hill; 2001; ISBN: 007026712X

[16] HERAEUS, *"Fused silica - a fascinating material"*; Heraeus Quartz America LLC, HQI Base Materials Division; 2400 Grand Avenue Pkwy, Suite 102, Austin, TX, 78728, USA; Homepage: http://heraeus-quarzglas.com

[17] HERING, MARTIN, STOHRER; "Physik fuer Ingenieure"; Springer, Berlin; ISBN: 3-540-66135-2; 1999; p.104

[18] ICSD – INORGANIC CRYSTAL STRUCTURE DATABASE. ©FIZ Karlsruhe, Germany and NIST, US Department of Commerce. Release 2004/2, entry 62404

[19] KUCHLING, HORST; "Physik - Formeln und Gesetze"; 21. Auflage; VEB Fachbuchverlag; Leipzig 1991

[20] LAUTERBORN, TIM; "Investigation of diffraction limited high power fiber amplifiers with adjustable pulse parameters", Diploma thesis, RWTH Aachen, 2004

[21] LIMPERT, J.; SCHREIBER, T.; LIEM, A. et al; "Thermo-optical properties of air-clad photonic crystal fiber lasers in high power operation"; Optics Express, vol.11, no.22; November 2003

[22] MARTIN, HOLGER; „Waermeuebertragung I" Thermische Verfahrenstechnik (TVT), Universitaet Karlsruhe; http://tvt.ciw.uni-karlsruhe.de; martin@tvt.uka.de

[23] MC.LACHLAN and MEYER; "Temperature dependence of the extinction coefficient of fused silica for CO2 laser wavelengths"; Applied Optics, Vol.26, Issue 9; May 1987; p. 1728

[24] MITRA, DIPL. PHYS. THOMAS; „Ablation biologischen Hartgewebes mit gepulsten IR-Lasern"; Dissertation; Heinrich-Heine Universität Düsseldorf; 2002

[25] MUNDRY, TOBIAS; "Einbrennsilikonisierung bei pharmazeutischen Glaspackmitteln - Analytische Studien eines Produktionsprozesses"; Dissertation at the Institut für Pharmazie of Humboldt Universität Berlin; 19.07.1999; http://edoc.hu-berlin.de/dissertationen/chemie/mundry-tobias/HTML/mundry-ch1.html

[26] NEUROTH N., ``Der Einfluß der Temperatur auf die spektrale Absorption von Gläsern im Ultraroten", *Glastechnische Berichte*, 25(8), July 1952; pp. 242-249

[27] NEUROTH N., ``Der Einfluß der Temperatur auf die spektrale Absorption von Gläsern im Ultraroten II", *Glastechnische Berichte*, 26(3), February 1953; pp. 66-69

[28] NEUROTH N., ``Der Temperatureinfluß auf die optischen Konstanten von Glas im Gebiet starker Absorption", *Glastechnische Berichte*, 28(11):411-422, November 1955

[29] OLSEN, D.A. & OSTERAAS, A.J.; "The Critical Surface Tension of Glass"; J. Phys. Chem. 68; 1964; pp. 2730-2732

[30] ONORATO, P.I.K. AND UHLMANN, D.R.; Journal of Non-Crystalline Solids; vol.22, no.2, 1976, pp.367-378

[31] ROFIN-SINAR UK LTD.; "Operating Manual ROFIN SCx10 OEM CO_2 Slab Laser"; August 2003

[32] ROSE, A.H.; "Devitrification in annealed optical fiber"; Journal of Lightwave Technology, vol.15, no.5; May 1997; pp.808-814

[33] SHNEIDMAN, V.A.; "Time-dependent nucleation during reheating of a rapidly quenched glass"; Journal of Chemistry and Physics, Vol. 102; Jan. 1995; pp. 1791-1795

[34] SOSMAN, ROBERT B.; "The Properties of silica : an introduction to the properties of substances in the solid non-conducting state"; Chemical Catalog Co., New York, 1927

[35] TOMOZAWA, M. AND DOREMUS, R.H. EDS.; Treatise on Materials Science and Technology, Vol. 17: Glass II; New York: Academic, 1979; pp. 41-113

[36] UHLMANN, D.R.; "A kinetic treatment of glass formation"; Journal of Non-Crystalline Solids; vol.7, no.4, 1972; pp.337-348

[37] WIBERG, N.; "Hollemann-Wiberg, Lehrbuch der Anorganischen Chemie"; Verlag Walter de Gruyter; Berlin, New York; 1985

[38] ZHANG, JIE; HERMAN, PETER R.; LAUER, CHRISTIAN ET.AL.; „157-nm Laser-Induced Modification of Fused-Silica Glasses"; Department of Electrical and Computer Engineering, University of Toronto, Toronto, ON M5S 3G4, Canada

Table of figures

Table of tables

Table of Symbols

Symbol	Used for	Value / SI-Unit
ρ	Density of Fused Silica	kg/m^3
k_{ex}	Extinction Coefficient	
α	Absorption Coefficient	m^{-1}
λ	Laser Wavelength	m
c_p	Specific Heat Capacity	$\frac{J}{kg \cdot K}$
T_m	Temperature of Melt	°C
T_n	Temperature at which the minimum cooling rate intersects the T-T-T diagram	°C
t_n	Time Corresponding to T_n	s
t_P	Total Process Time	s
η	Dynamical Viscosity Coefficient	$Pa \cdot s$ (or $P = 1/10\, Pa \cdot s$)
p_i	Internal Pressure	Pa
σ_T	Surface Tension	N
x_P	Pulse Overlap	% of $d(z)$
P_{AV}	Laser Output Power	W
P_L	Pulse Power	W
ΔP_{AV}	Power Stability	%

f	Focal length of scanner lens	*m*
θ_0	Beam Divergence	*rad*
d_L	Beam Diameter (1/e²)	*m*
k	Wavenumber	m^{-1}
θ_F	Divergence of focused beam (full angle)	*rad*
z_R	Rayleigh Length	*m*
$E(r,z)$	Electrical Field Force Distribution	V/m
$d(z)$	Beam Diameter	*m*
d_F	Fiber Diameter	*m*
d_S	Beam diameter on surface	*m*
d_H	Hole Diameter	*m*
d_D	Disc Diameter	*m*
h_F	Height of fiber above Disc	*m*
h_D	Thickness of Disc	*m*
v_s	Scanning Speed	*m/s*
d_C	Diameter of scanned circle	*m*
z_F	Focus position	*m*
d_0	Beam diameter in focus	*m*
P_σ	Radiation Losses	*W*
σ	Stefan Bolzman Constant	$5.67 \cdot 10^{-8} \frac{W}{m^2 K^4}$

A_σ	Active Area of Radiation	m^2
T_{FS}	Glass Temperature	K
T_S	Temperature of Surrounding	K
P_α	Convection Losses	W
α_C	Conductive Heat Transfer Coefficient	$\frac{W}{m^2 K}$
A_α	Active Area of Convection	m^2
$A_{C\min}$	Inner cross sectional area for heat conduction	m^2
$A_{C\max}$	Outer cross sectional area for heat conduction	m^2
κ	Thermal Diffusivity	m^2/s
Δ	Laplacian (grad div = ∇^2)	
∇	Nabla Operator $\left(d/dx, d/dy, d/dz\right)$	
λ_{FS}	Thermal Conductivity	$\frac{W}{m \cdot K}$
P_λ	Conduction Losses	W
A_λ	Cross Sectional Area of Conduction	m^2
l_λ	Length of Conduction	m
A_{melt}	Surface Area of the melt	m^2
r_{melt}	Radius to which the disc is melted	m

m_{melt}	Mass of Melt	*kg*
β	Absorption Depth	*m*
τ_R	Thermal Relaxation Time	*s*
ϑ_{f1}	Working Point	*P*
ϑ_{f2}	Softening Point	*P*
ϑ_{f3}	Annealing Temperature	*P*
ϑ_{f4}	Strain Point	*P*
σ_T	Surface Tension	N/m
r_1, r_2	Main radii of curvature in a liquid	*m*
K	Beam Propagation Factor	*unit less*
PP	Pulse Period	*s*
PW	Pulse Width	*s*
DC	Duty Cicle	*%*
P_{AV}	Average Laser Power	*W*